Simulation of Impact Penetration and Perforation of Metal Targets Using the Smoothed Particle Galerkin Method

Youcai Wu, Ph.D.[1]; and C. T. Wu, Ph.D.[2]

Abstract: This paper applies the smoothed particle Galerkin (SPG) method to the analysis of penetration and perforation of metal targets. The SPG weak form is integrated using the direct nodal integration (DNI) technique with a nonresidual penalty–type stabilization term derived from strain smoothing. An adaptive anisotropic Lagrangian kernel is used to model the large deformation in the penetration and perforation processes. To model material breakup and fragmentation while avoiding potential spurious self-healing of meshfree approximations used in the failure analysis, a strain-based bond failure mechanism is implemented and the sensitivity to the failure criterion is numerically investigated. Two experiments are analyzed using the SPG formulation. The numerical results are compared with the experimental data to evaluate the effectiveness of the present method. The convergence behavior of the SPG formulation is also studied. **DOI: 10.1061/(ASCE)EM.1943-7889.0001470.** *© 2018 American Society of Civil Engineers.*

Author keywords: Smoothed particle Galerkin (SPG); Impact; Penetration; Perforation; Metal.

Introduction

Impact penetration and perforation occur in many situations, from low velocity to hypervelocity, such as a projectile impacting heavy armor, warhead-launched fragments from detonation of cased explosives impacting neighboring structures, micrometeoroids colliding with spacecraft, and so on. Therefore, understanding and predicting the high strain rate nonlinear structural responses and material failure in such impact processes is crucial to the design of protective systems. Research on various aspects of impact phenomena has been carried out for decades, such as predicting the depth of penetration (DOP); perforation exit velocity; failure modes of targets (e.g., stretching, bending, spalling, petalling, discing, and plugging); and the effect of the nose shape and aspect ratio of projectiles, the material responses of projectiles and targets, and so on. In general, three approaches, namely experimental (Chandel et al. 2012; Pedersen and Bless 2006; Orphal et al. 1997; Xiao et al. 2017; Rajendran 1998; Sorensen et al. 1991; Roy et al. 2016; Schwer 2009; Bishop et al. 1945; Goodier 1964; Golsdmith and Finnegan 1971; Dikshit and Sundararajan 1992; Hohler et al. 1995; Orphal and Franzen 1997; Forrestal and Luk 1992), semianalytical (including empirical and semiempirical) (Bishop et al. 1945; Goodier 1964; Golsdmith and Finnegan 1971; Dikshit and Sundararajan 1992; Hohler et al. 1995; Orphal and Franzen 1997; Forrestal and Luk 1992; Ben-Dor et al. 2005; Lu and Wen 2018; Li and Chen 2003; Forrestal et al. 1995; Sataphathy 2001; Nechitailo 2015), and numerical (Xiao et al. 2017; Rajendran 1998; Sorensen et al. 1991; Roy et al. 2016; Schwer 2009; Sherburn et al. 2015; Lacerda and Lacome 2001; Asadi Kalameh et al. 2012; Wu et al. 2014b, 2016c; Wu et al. 2017b;

Randles et al. 1995; Fahrenthold and Horban 2001; Fountzoulas et al. 2007) methods, have been reported. For instance, based on experimental data, Bishop et al. (1945) developed equations to estimate forces on conical nose punches pushed slowly into metal targets; Goodier (1964) developed a model to predict the DOP of rigid spheres penetrating into metal targets; Forrestal et al. (1995) developed closed-form penetration equations for rigid, spherical-nose rods impacting ductile metal targets; Li et al. (2003) developed dimensionless formulas for the DOP of concrete targets impacted by a nondeformable projectile; and Nechitailo (2015) developed analytical solutions to compute the maximum DOP of various impactors penetrating soil targets. Ben-Dor et al. (2005) presented a comprehensive review of the advances in analytical modeling of ballistic impact.

Although semianalytical approaches for ballistic impact dynamics have been developed over many years, their application is quite limited because these approaches do not include the physics during high strain rate impact processes, and hence the solution is usually inaccurate and nonobjective. To reduce the experimental cost and to optimize the design of protective structures, it is very important to accurately predict responses in impact penetration and perforation processes. Therefore, effort has also been spent on the development and application of accurate numerical schemes using high-fidelity physics-based simulations. The finite-element method (FEM) with element erosion technique (Johnson and Stryk 1987; Belytschko and Lin 1987) was an early effort in this regard and it is still used in some analyses (Xiao et al. 2017; Rajendran 1998). However, the phenomenological failure criterion of the element erosion technique is ad hoc and nonunique. Eulerian approaches with fixed grids are also applied (Sorensen et al. 1991; Roy et al. 2016; Schwer 2009; Liden et al. 2012) in the analysis of impact phenomena due to their capability of modeling large deformation and flow. Nonetheless, due to the use of fixed grids and poor performance in advection of constitutive model state variables, such as those used in modeling soil and concrete, Eulerian approaches have difficulties detecting the new surface formation, which limits their application to problems in which material breakup dominates.

Compared with the FEM, meshfree methods are more applicable in modeling large deformation (Chen et al. 1996; Li and Liu 2004) and material failure with separation (Simkins and Li 2006)

[1]Senior Scientist, Livermore Software Technology Corporation, 7374 Las Positas Rd., Livermore, CA 94551 (corresponding author). Email: ycwu@lstc.com

[2]Senior Scientist, Livermore Software Technology Corporation, 7374 Las Positas Rd., Livermore, CA 94551. Email: ctwu@lstc.com

problems because meshfree approximations do not rely on structured mesh topology. The smoothed particle hydrodynamics (SPH) method is considered the earliest meshfree method, and was introduced by Lucy (1977) and Gingold and Monaghan (1977) for modeling astrophysical and cosmological problems. In this method, the governing partial differential equations are transformed into integral equations, and kernel estimations are applied to the approximation of field variables (e.g., displacement or velocity). This method was demonstrated to work well for solving fluid-like problems that historically were reserved for Eulerian approaches (Violeau 2012). However, various numerical deficiencies (Belytschko et al. 2000; Rabczuk et al. 2004) have been encountered in extending the SPH method to solid mechanics problems with finite domains, such as lack of consistency, tension instability, low-energy modes, dispersive wave propagation, and difficulty in enforcing essential boundary conditions. In spite of these deficiencies, the SPH method is still one of the most popular numerical methods for simulating the severe deformation and material separation in many impact problems involving metallic targets (Roy et al. 2016; Lacerda and Lacome 2001; Asadi Kalameh et al. 2012; Mohotti et al. 2015; Ibne Islam et al. 2017; Plassard et al. 2011) because no better approach has been available, although some other meshfree methods, such as the material point method (MPM) and the discrete-element method (DEM), occasionally have been applied in the analysis of penetration and perforation of metallic targets (Zhang et al. 2006; Huang et al. 2011; Watson and Steinhauser 2017).

To resolve the aforementioned SPH issues, the element-free Galerkin (EFG) method (Belytschko 1994) and reproducing kernel particle method (RKPM) (Liu et al. 1995) were developed. Subsequently, to alleviate the low-energy modes in the direct nodal integration (DNI) scheme, which is used in the SPH method, Chen et al. (2001) introduced the stabilized conforming nodal integration (SCNI) method. The SCNI has also been generalized for beam (Wang and Chen 2006), plate (Wang and Chen 2004; Nguyen-Xuan et al. 2008; Wang and Peng 2013), and solid finite-element formulations (Liu et al. 2007) in the last decade. To further enhance the integration accuracy, Chen et al. (2013) derived arbitrary-order Galerkin exactness for the SCNI technique under the framework of variational consistency. However, it is cumbersome to construct the conforming integration cells in failure analysis due to the formation of new surfaces. Therefore, the SCNI algorithm was simplified to the stabilized nonconforming nodal integration (SNNI) scheme (Puso et al. 2008) so that it can be applied to extremely large deformation with material failure including separation analysis. The SNNI scheme has been successfully applied to modeling concrete and soil failure and separation problems (Sherburn et al. 2015; Guan et al. 2009).

Although the SCNI/SNNI integrated meshfree formulations have been successfully applied in many material failure and separation analyses (Sherburn et al. 2015; Wu et al. 2014a, b, 2016c; Guan et al. 2009; Wang and Li 2013), its requirement of a background mesh or smoothing cells for domain integration has posed some limitations on their application. Additionally, most meshfree methods remain challenging in tracking the formation of new surfaces and preventing material self-healing. Therefore, a genuine meshfree method, the smoothed particle Galerkin (SPG) method (Wu et al. 2015a, b, 2016a, b, 2017a) was recently developed for modeling material failure and separation. The SPG method is a residual-based Galerkin meshfree method. Its weak form is integrated using the direct nodal integration (DNI) technique to improve computational efficiency. A strain operator derived from displacement smoothing theory is used in the SPG formulation for stabilizing the DNI scheme. In the ensuing development

(Wu et al. 2015b, 2016b), a penalty-based h^2-stabilization formulation was developed using a strain operator derived from direct strain smoothing. This stabilization formulation is parameterized by a measure of the local length scale without using a stabilization control parameter. As such, the SPG formulation has been applied to the analysis of damage-induced strain localization in elastic materials (Wu et al. 2015b), ductile fracture in two-dimensional explicit dynamics (Wu et al. 2016b), three-dimensional concrete perforation and penetration (Wu et al. 2017b), and three-dimensional destructive metal grinding applications (Wu et al. 2017a).

This paper extends the SPG formulation to the analysis of impact penetration and perforation phenomena for metal targets and projectiles in which the deformation of the projectile is also included. The remainder of the paper is organized as follows. The weak form and the corresponding three-dimensional semidiscrete formulations of the smoothed particle Galerkin (SPG) method for large deformation analysis are presented in the "Overview of SPG Method" section; the "Mechanism for Severe Deformation and Material Failure" section presents the adaptive anisotropic Lagrangian kernel used in the three-dimensional formulation for severe deformation and the strain-based bond failure mechanism for metal material breakup; the "Numerical Example" section analyzes two experiments and investigates convergence study and failure criterion sensitivity; and concluding remarks are made in the "Conclusion."

Overview of SPG Method

Weak Form Formulations

The SPG weak form is based on the penalty method (Wu et al. 2015a, b, 2016a) to find $\hat{\boldsymbol{u}} \in \boldsymbol{H}_g^1(\Omega) = \{\boldsymbol{v}:\boldsymbol{v}|_\Omega \in \boldsymbol{H}^1(\Omega), \boldsymbol{v} = \boldsymbol{v}_g$ on $\Gamma_g\}$ such that

$$
\int_{\Omega^0} \delta\hat{\boldsymbol{u}} \cdot \rho^0 \ddot{\hat{\boldsymbol{u}}} d\Omega^0
$$
$$
= \underbrace{\int_{\Omega_c^0} \delta\boldsymbol{F}^T : \boldsymbol{P}(\boldsymbol{F}) d\Omega_c^0}_{\text{standard term}} + \underbrace{\int_{\Omega^0} \delta\tilde{\boldsymbol{F}}^T : \tilde{\boldsymbol{P}}(\tilde{\boldsymbol{F}}) d\Omega^0}_{\text{penalty term}} - l^{\text{ext}}(\hat{\boldsymbol{u}}),
$$
$$
\forall\ \delta\hat{\boldsymbol{u}} \in \boldsymbol{H}_0^1 = \{\boldsymbol{v}:\boldsymbol{v}|_\Omega \in \boldsymbol{H}^1(\Omega), \boldsymbol{v} = \boldsymbol{0}\ \text{on}\ \Gamma_g^0\} \tag{1}
$$

where Ω^0 = initial domain occupied by the material; ρ^0 = initial material density; and Γ_g = Dirichlet boundary applied with Dirichlet boundary conditions.

The variation of deformation gradient $\boldsymbol{F}$ and enhanced deformation gradient $\tilde{\boldsymbol{F}}$ for stabilization are defined as

$$
\delta\boldsymbol{F} = \delta\left(\frac{\partial\boldsymbol{x}}{\partial\boldsymbol{X}}\right) = \frac{\partial\delta\hat{\boldsymbol{u}}}{\partial\boldsymbol{X}} \tag{2}
$$

$$
\delta\tilde{\boldsymbol{F}} = \nabla(\delta\boldsymbol{F}) \cdot \boldsymbol{\lambda}^b(\boldsymbol{X}) \quad \forall\ \boldsymbol{X} \in \Omega^0 \tag{3}
$$

$$
\boldsymbol{\lambda}^b(\boldsymbol{X}) = \int_{\Omega^0} \tilde{\Psi}^b(\boldsymbol{X};\boldsymbol{X}-\boldsymbol{\xi})(\boldsymbol{\xi}-\boldsymbol{X}) d\Omega \tag{4}
$$

where $\boldsymbol{x}$ = coordinates in the current configuration; $\boldsymbol{X}$ = coordinates in the reference configuration; $\tilde{\Psi}^b$ = strain smoothing function (Wu et al. 2015b, 2016a) with a kernel support size of b for stabilization in the SPG method; and $\boldsymbol{\lambda}^b$ = coefficient matrices for stabilization.

The external force is given as

$$
l^{ext}(\hat{\boldsymbol{u}}) = \int_{\Omega^0} \delta\hat{\boldsymbol{u}} \cdot \boldsymbol{b} d\Omega^0 + \int_{\Gamma_h^0} \delta\hat{\boldsymbol{u}} \cdot \boldsymbol{h}^0 d\Gamma_h^0 \tag{5}
$$

where b = body force; and h^0 = surface traction applied on the Neumann boundary Γ_h^0.

The field variables $\hat{u}$ are approximated using the meshfree method (Belytschko et al. 1994; Liu et al. 1995) as

$$u^h(X, t) = \sum_{I=1}^{NP} \Phi_I^a(X) u(X_I, t) = \hat{u}(X, t) \quad \forall\, X \in \Omega^0 \quad (6)$$

where $\Phi_I^a(X)$ $(I = 1, \ldots, NP)$ = meshfree shape functions (Belytschko et al. 1994; Liu et al. 1995) with a kernel support size of a; NP = number of nodes used in the domain discretization; and $u(X_I, t)$ = generalized displacement (Chen et al. 1996) of particle I in the Galerkin meshfree method.

In Eq. (1), P denotes the nominal stress which can be related to the Cauchy stress σ in metal plasticity by

$$P = J^0 F^{-1} \cdot \sigma \quad (7)$$

where J^0 = determinant of the deformation gradient F.

The penalty functional for the second term in the right-hand side (RHS) of Eq. (1) contains an enhanced stress field $\tilde{P}$ for stabilization. The enhanced Cauchy stress field for stabilization in small strain analysis is formulated using a material response tensor (elastoplastic tangent modulus) C^σ as (Wu et al. 2015b, 2016b)

$$\tilde{\sigma} = C^\sigma : (\nabla \varepsilon(\hat{u}) \cdot \lambda^b) \quad (8)$$

Consequently, the enhanced nominal stress for stabilization can be expressed by

$$\tilde{P} = J^0 F^{-1} \cdot \tilde{\sigma} \quad (9)$$

The strain smoothing function $\tilde{\Psi}^b$ can be different from the meshfree shape function $\Phi_I^a(X)$, in general. However, for simplicity and efficiency, this paper takes the strain smoothing function as exactly the same meshfree shape function.

Semidiscrete Formulations

Using the first-order meshfree convex approximation (Wu et al. 2011; Wu and Koishi 2012) for $\Phi^a(X)$ and zeroth-order strain smoothing function for $\tilde{\Psi}^b(X)$ leads to the following semidiscrete form of the momentum equation [Eq. (1)] to be solved in explicit dynamics analysis:

$$M^{lump} \ddot{U} = f^{ext} - f^{int} - \tilde{f}^{stab} \quad (10)$$

$$M_I^{lump} = \sum_{N=1}^{NP} \rho^0 \phi_I^a(X_N) V_N^0 I_{[3\times3]} \quad (11)$$

where $f^{ext} = (f_1^{ext}, \ldots, f_{NP}^{ext})^T$ = standard external force matrix; $\ddot{U} = (\ddot{U}_1, \ldots, \ddot{U}_{NP})^T$ = matrix containing nodal accelerations; V_N^0 = initial nodal volume of node N; and M_I^{lump} = lumped nodal mass matrix of node I.

Using the particle integration (DNI) scheme, the internal force and stabilization force are computed by

$$f_I^{int\,DNI} \stackrel{.}{=} \sum_{N=1}^{NP} \mathcal{B}_I^T(X_N) P(X_N) V_N^0 \quad \forall\, X_N \in \Omega^0 \quad (12)$$

$$\tilde{f}_I^{stab\,DNI} \stackrel{.}{=} \sum_{N=1}^{NP} \tilde{\mathcal{B}}_I^T(X_N) \tilde{P}(X_N) V_N^0 \quad (13)$$

The nominal stress P defined with respect to the reference configuration in Eq. (12) can be expressed by the Cauchy stress σ for convenience in metal plasticity computations. Using the Voigt rule, the internal force can be calculated by

$$f_I^{int\,DNI} \stackrel{.}{=} \sum_{N=1}^{NP} \mathcal{B}_I^T(X_N) P(X_N) V_N^0 = \sum_{N=1}^{NP} B_I^T(X_N) \sigma(X_N) J^0 V_N^0 \quad (14)$$

Similarly, the stabilization force can be expressed as

$$\tilde{f}_I^{stab\,DNI} \stackrel{.}{=} \sum_{N=1}^{NP} \tilde{\mathcal{B}}_I^T(X_N) \tilde{P}(X_N) V_N^0 = \sum_{N=1}^{NP} \tilde{B}_I^T(X_N) \tilde{\sigma}(X_N) J^0 V_N^0 \quad (15)$$

where the components of the strain-gradient matrices $\mathcal{B}_I$, $\tilde{\mathcal{B}}_I$, B_I, and $\tilde{B}_I$ were given by Wu et al. (2017a), and thus they are omitted from this paper.

The Cauchy stress is updated objectively in the standard way according to Simo and Hughes (1986) because the large deformation analyses in this paper use constitutive equations based on the Jaumann stress rate.

Eq. (10) is temporally integrated by the Newmark method. The critical time step for the central difference time integration in explicit dynamics analysis is governed by the Courant-Friedrichs-Lewy (CFL) condition and is determined following the developments in Wu et al. (2015b, 2016a, b, 2017b) and Park et al. (2011). The meshfree time step in explicit dynamics analysis is controlled (Wu et al. 2015b, 2016a, b, 2017b; Park et al. 2011) by the radius size a of $\Phi^a(X)$ in the displacement approximation, instead of the closest nodal distance or element size as in the FEM; therefore they are not reduced abruptly due to severe material deformation.

Mechanisms for Severe Deformation and Material Failure

Adaptive Anisotropic Lagrangian Kernel

To treat the large deformation situations that are beyond the applicability of the standard Lagrangian approach, an adaptive anisotropic Lagrangian kernel was developed (Wu et al. 2016a). Using the chain rule, the calculation for the deformation gradient in Eq. (2) can be rewritten (Wu et al. 2016a, 2017b) as

$$F^{n+m} = \widehat{F}^{n+m} F^n \quad (16)$$

where $\widehat{F}^{n+m}(\hat{x})$ = decomposed deformation gradient, from $t = t_n$ to t_{n+m}, computed in the new reference configuration $\widehat{X} = x(X, t_n)$ and is given by

$$\begin{aligned}
\widehat{F}_{ij}^{n+m}(X_J) &= \frac{\partial \hat{x}_i}{\partial \widehat{X}_j} = \sum_{I=1}^{NP} \frac{\partial \Phi_I^a(\widehat{X}_J)}{\partial \widehat{X}_j} \hat{x}_{iI}(X, t_{n+m}) \\
&= \sum_{I=1}^{NP} \frac{\partial \Phi_I^a(\widehat{X}_J)}{\partial \widehat{X}_j} (\widehat{X}_{iI} + \tilde{u}_{iI}(X, t_{n+m})) \\
&= \delta_{ij} + \sum_{I=1}^{NP} \frac{\partial \Phi_I^a(\widehat{X}_J)}{\partial \widehat{X}_j} \tilde{u}_{iI}(X, t_{n+m}) \quad (17)
\end{aligned}$$

where $\hat{x} = \widehat{X} + \tilde{u}(X, t_{n+m})$ is a position vector defined in the new reference configuration $\widehat{X} = x(X, t_n)$. A local $\widehat{X}^I$-coordinate system whose axes are parallel to the global Cartesian coordinate system and whose origin is located at $\widehat{X}_I$ is defined for each meshfree node I. In each new reference configuration, an ellipsoidal

nodal support is defined for neighbor particle searching. The three-dimensional ellipsoidal cubic spline kernel function ϕ_I^a is defined in another local $\widehat{\widehat{X}}^I$-coordinate system by

$$\phi_I^a(\widehat{X}_J) = \phi_1\left(\frac{\widehat{\widehat{X}}_J^I}{h_1^n}\right)\phi_1\left(\frac{\widehat{\widehat{Y}}_J^I}{h_2^n}\right)\phi_1\left(\frac{\widehat{\widehat{Z}}_J^I}{h_3^n}\right) \quad (18)$$

where h_1^n, h_2^n, and h_3^n = semimajor axes of the ellipsoid; $\widehat{\widehat{X}}_J^I$, $\widehat{\widehat{Y}}_J^I$, and $\widehat{\widehat{Z}}_J^I$ = projections of relative position vector $\widehat{X}_J - \widehat{X}_I$ on the local $\widehat{\widehat{X}}^I$-coordinate system, respectively; and ϕ_1 = standard one-dimensional cubic spline kernel function. Wu et al. (2016a, 2017b) gave more details regarding the anisotropic adaptive Lagrangian kernel, and therefore they are not repeated herein.

Strain-Based Particle Bond Failure

Even with the introduction of an anisotropic adaptive Lagrangian kernel, excessive straining may inevitably occur under severe deformation in impact simulations. Unlike the numerical treatment in an Eulerian approach, the excessive straining in a Lagrangian approach eventually causes numerical breakdown due to unavoidable negative Jacobians of the deformation gradient defined in Eq. (16).

To prevent this numerical artifact, and to model the material failure in three-dimensional metal impact analysis, an introduction of a discontinuity in the displacement field is considered. This is done by incorporating a strain-based bond failure mechanism. This numerical treatment is similar to the bond failure in peridynamics (Wu and Ren 2015; Silling and Askari 2005). The application of the SPG bond failure mechanism in metal impact analysis considers two neighboring particles that become disconnected during the neighbor particle searching whenever their averaged effective plastic strain and relative stretching reach their critical values respectively. In other words, the three-dimensional ellipsoidal cubic spline kernel function in Eq. (18) for a pair of particles I and J can be redefined as

$$\phi_I^a(\widehat{X}_J) = \begin{cases} 0 & \text{if } \varepsilon_{IJ}^p > \varepsilon_{crit}^p \text{ and } e > e_{crit} \\ \phi_1\left(\frac{\widehat{\widehat{X}}_J}{h_1^n}\right)\phi_1\left(\frac{\widehat{\widehat{Y}}_J}{h_2^n}\right)\phi_1\left(\frac{\widehat{\widehat{Z}}_J}{h_3^n}\right) & \text{otherwise} \end{cases}$$
$$(19)$$

where

$$\varepsilon_{IJ}^p = \frac{\varepsilon_{eff}^p(\widehat{X}_I) + \varepsilon_{eff}^p(\widehat{X}_J)}{2} \quad (20)$$

$$e = \frac{\|x_J - x_I\|}{\|X_J - X_I\|} \quad (21)$$

where ε_{eff}^p = effective plastic strain; ε_{crit}^p = critical value of effective plastic strain; and e_{crit} = critical value of nodal pair extension for the bond failure in metals. The input of $e_{crit} \geq 1.0$ guarantees that the SPG bond does not fail under compression in metals.

Fig. 1 illustrates the SPG bond failure mechanism. The large circle marked supp(x_k) represents the support of Node K, and the large circle marked supp(x_l) represents the support of Node I. Initially, five bonds are connected to Node K, i.e., Bond KI, Bond KJ, and three other bonds between Node K and the three small circles. Seven bonds are connected to Node I. If the failure criteria for Bond KI are satisfied, i.e., $\varepsilon_{KI}^p > \varepsilon_{crit}^p$ and $e > e_{crit}$, Bond KI is broken. Therefore, $\phi_K^a(\widehat{X}_I) = 0$ and $\phi_I^a(\widehat{X}_K) = 0$. However,

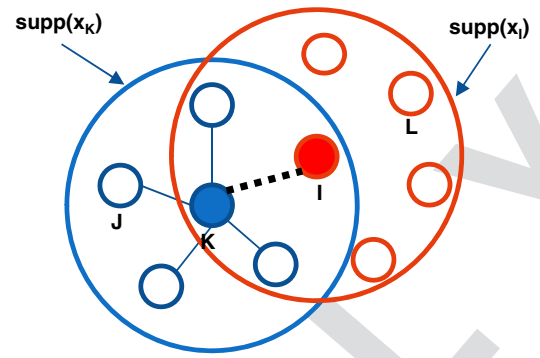**Fig. 1.** Illustration of SPG bond failure mechanism.

$\phi_K^a(\widehat{X}_J) \neq 0$ and $\phi_I^a(\widehat{X}_L) \neq 0$, which means Bonds KJ and IL are still connected. This indicates that the state variables (i.e., stress and strain) at Nodes K and I are still able to evolve regularly according to the deformation and material law. The only change is that their neighboring particles have one less node. Therefore, unlike the finite-element failure mechanism, in which the element is deleted (loss of mass) according to an ad hoc erosion criterion and the element stress is set to zero (loss of momentum) when failure occurs, the SPG bond failure mechanism preserves the mass and momentum.

Because the effective plastic strain at each particle monotonically increases during the course of deformation, the kinematic disconnection between two particles in a pair is considered as a permanent and irreversible process. This is a substantial characteristic of the present method in metal penetration and perforation applications because the failure analysis completely excludes the nonphysical material self-healing issue. Once the bond between two particles is broken, the interaction between the two particles is treated by the self-contact algorithm introduced by Wu et al. (2017b), and thus the debris can be contained in the penetration and perforation path rather than flying everywhere unphysically.

Numerical Example

This section analyzes two examples and compares them with experimental data to evaluate the performance of the proposed SPG formulation, which was implemented in commercial software LS-DYNA (Hallquist 2006). The convergence of the algorithm and the sensitivity to the failure criterion were studied through the numerical analyses as well.

Unless otherwise specified, a normalized nodal support size of 1.5 was used for the displacement approximation and stabilization for all calculations. The adaptive anisotropic Lagrangian kernel described in the "Mechanism for Severe Deformation and Material Failure" section was updated constantly every 30 explicit time steps.

Perforation of Aluminum Plate

Schwer (2009) reported a series of metal plate impact experiments using various projectiles. The present study used a 6061-T6 aluminum plate $203 \times 203 \times 12.7$ mm as the target (Fig. 2). Two opposite edges of the plate were clamped. The plate was impacted by a blunt projectile perpendicular to the surface at the center. The projectile had a diameter of 16.7 mm, a length of 24.7 mm, and a short length of reduced-diameter shoulder (not shown). To simplify the model but maintain the mass of the projectile, it was modeled as a
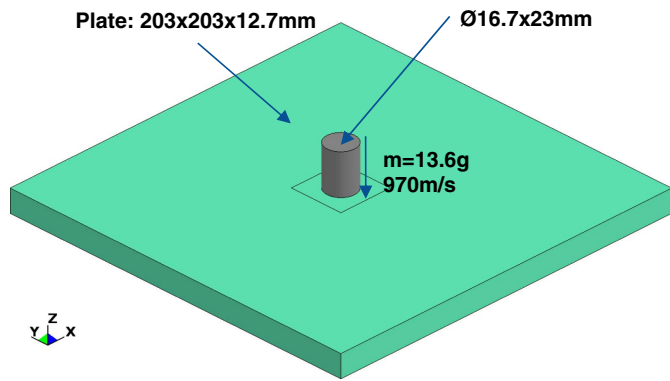
F2:1 **Fig. 2.** Plate perforation: geometry.

Ø16.7 × 23-mm cylinder. The projectile had a mass of 13.6 g and impacted the target plate at a velocity of 970 m/s. The friction coefficient between the projectile and the target was 0.30 (www .engineeringtoolbox.com). In the experiment, the projectile perforated the plate with a residual velocity of 344 m/s.

To save computational costs, only the vicinity (30 × 30 mm) of the impact region in the target was modeled by the proposed SPG formulation, whereas the remaining majority was modeled by FEM because much less deformation occurred in those regions. Wu et al. (2017a) identified the feasibility of this discretization. To study the convergence behavior, four discretizations were used (Fig. 3). The nodal distances in these four discretizations were 1.6, 1.0, 0.75, and 0.5 mm. The Johnson–Cook model (Johnson and Cook 1983) was used for the constitutive modeling of the target plate.

The parameters were taken from Schwer (2009). However, the Johnson–Cook damage law was not used, because the Johnson–Cook damage law is intended to fail the elements in a continuous sense by removing elements in the finite-element approach, which is not physical. On the other hand, a bond failure in SPG does not remove material from the calculation. The SPG bond failure criteria was $\varepsilon^p_{crit} = 0.4$ in this study. This value was determined by to a simple tension test using FEM with the Johnson–Cook damage law. Because continuum damage mechanics is not used in the Johnson–Cook model for metal impact analysis, the damage-induced strain localization and thus the mesh sensitivity problem (Wu et al. 2015b, 2016b) were not an issue in this study. The projectile was modeled by FEM with kinematic hardening plasticity with a yielding stress of 324 MPa and a hardening parameter of 150 MPa, but material failure was not considered for the projectile.

Figs. 4 and 5 show the velocity histories of the projectile obtained by the SPG and FEM with erosion analyses, respectively. The failure criterion for FEM with erosion analysis was an effective plastic strain of 0.4. The legend indicates the nodal distance in the discretization. The SPG residual velocity converged to the test data as the discretization was refined. In fact, the solution had nearly no discretization dependence as long as it was fine enough to propagate the high frequency impact wave properly (the poor solution for the 1.6 mm discretization was because that discretization was too coarse to propagate the impact wave). The results indicate that the SPG solution is convergent and is more accurate than FEM. Furthermore, the FEM solution did not converge uniformly with the discretization.

Fig. 6 illustrates the evolution of the effective plastic strain and the process of material failure and separation for the discretization with nodal distance of 1.0 mm on a cross section cut through the

(a)

(b)

(c)

(d)
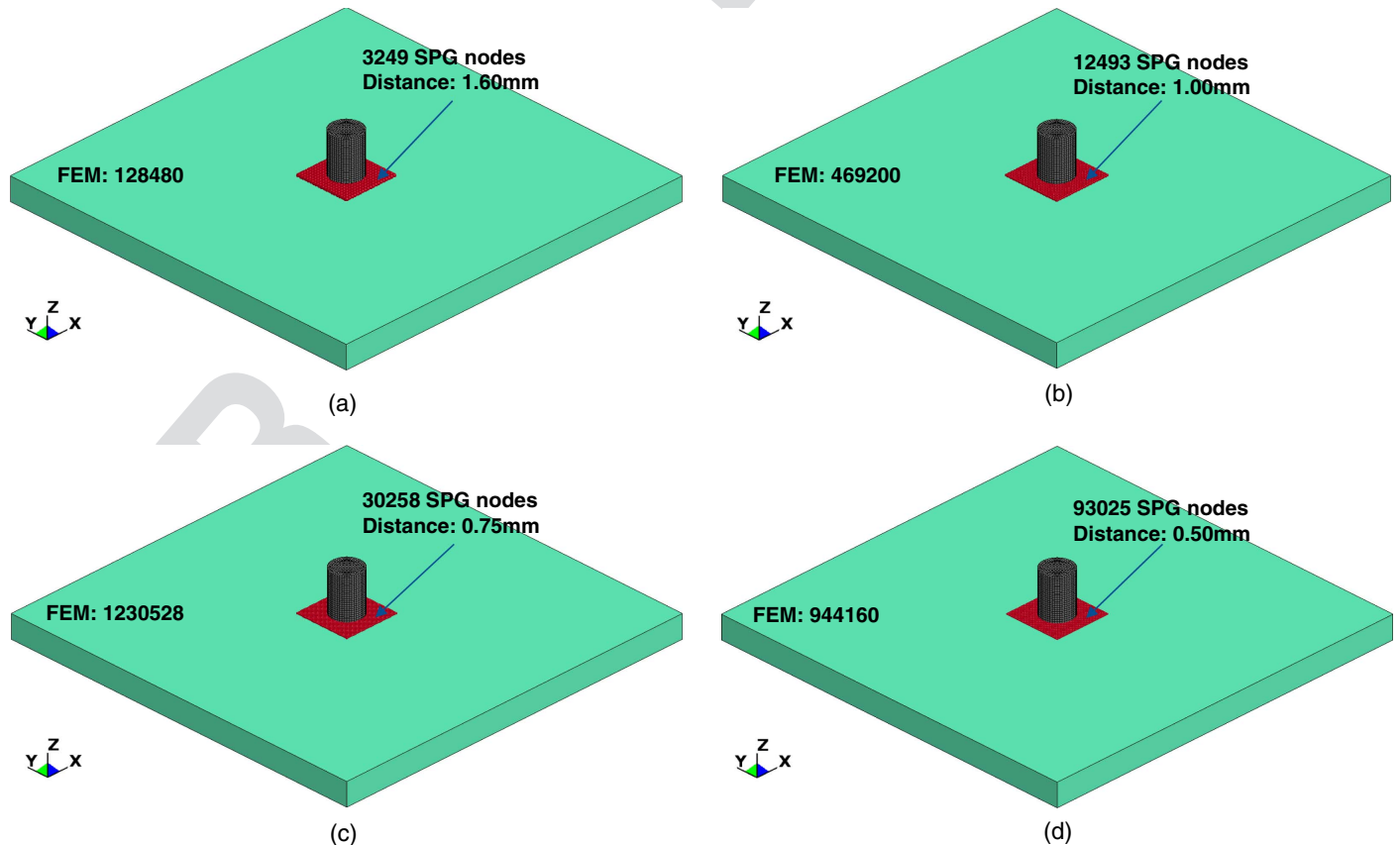
F3:1 **Fig. 3.** Plate perforation: discretizations.
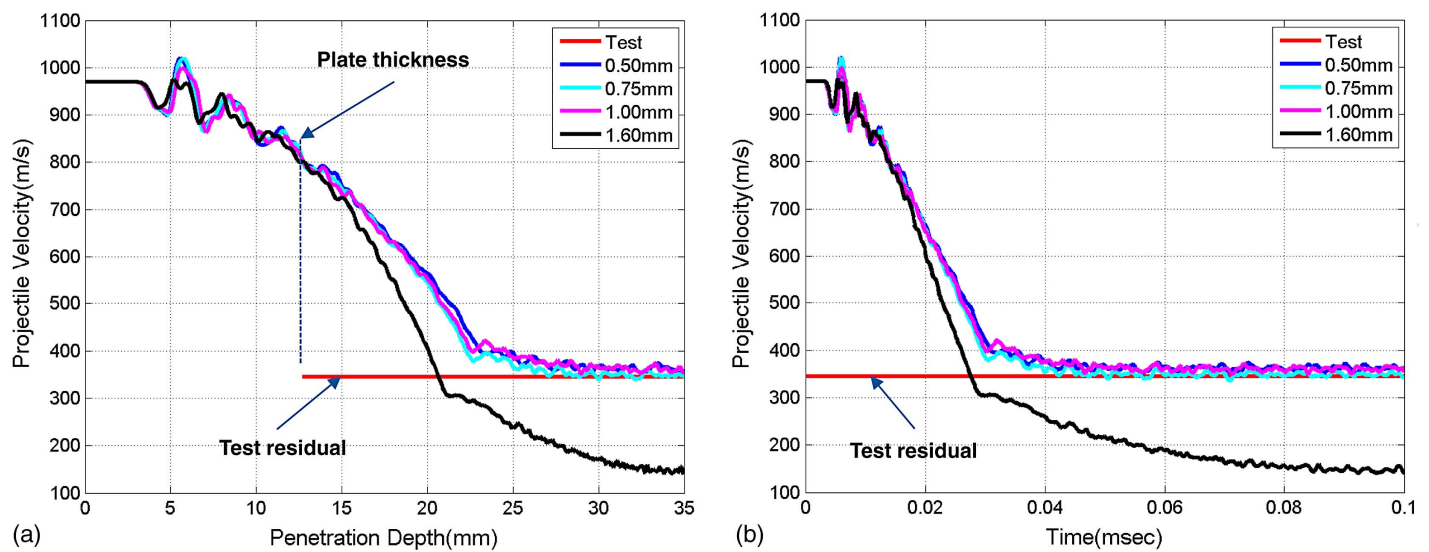
F4:1   **Fig. 4.** Plate perforation: projectile velocity history, SPG solution.
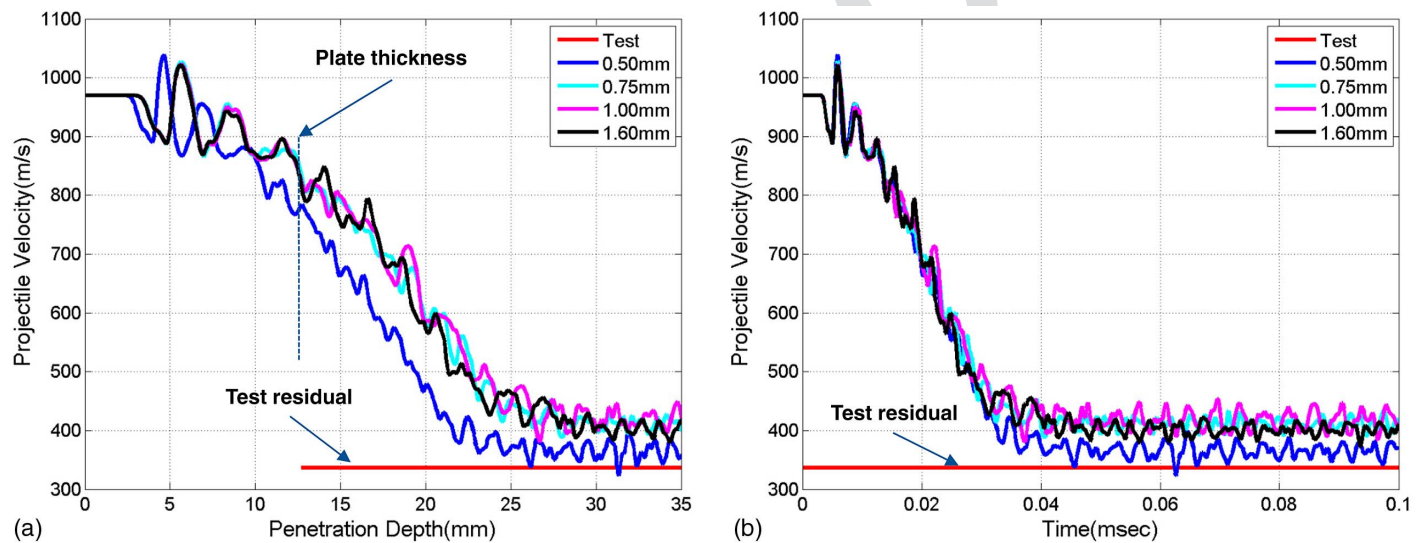

F5:1   **Fig. 5.** Plate perforation: projectile velocity history, FEM solution.

392   midplane. Material failure and separation was clearly seen during
393   the process of impact. Both ejecta and debris chips were observed
394   as well.

395   Fig. 7(a) shows the side view of the perforated plate after the
396   experimental test, and Figs. 7(b–d) show the side view of the per-
397   forated plates at termination for various target discretizations. Small
398   shear lips were observed in the numerical results. Fig. 8 shows the
399   perforated target plate and Fig. 9 shows the deformed projectile for
400   various target discretizations. In general, the deformed shapes were
401   qualitatively consistent with the experimental observations.

Sensitivity Study

402

403   This section investigates the impact on the perforation response of
404   the coefficient of friction (COF), the failure criterion (FS), and the
405   size of SPG zone by using the discretization with nodal distance
406   0.75 mm. Unless otherwise specified, the bond failure criteria of
407 $\varepsilon_{crit}^p = 0.4$ was used.

Influence of Coefficient of Friction

408

Fig. 10 shows the projectile velocity histories obtained using   409
the SPG formulation for various COFs for the discretization in   410
Fig. 3(c). Both solutions were close to the test data and showed that   411
a larger residual velocity is obtained when a smaller COF is used,   412
which is physical. The difference between the numerical solution   413
and the experimental data increased from 1 to 6% when the COF   414
decreased from 0.3 to 0.2. The COFs used herein were static, which   415
might not be proper for this type of dynamic problem. However,   416
calibrating a proper COF so that the numerical solution matched   417
the test data was beyond the scope of this study.   418

Sensitivity to Failure Criterion

419

Fig. 11 shows the projectile velocity histories obtained using the   420
SPG formulation for bond failure criteria $\varepsilon_{crit}^p = 0.4$ and $\varepsilon_{crit}^p = 0.2$ 421
for the discretization in Fig. 3(c). The difference between the   422
numerical solutions was marginal.   423
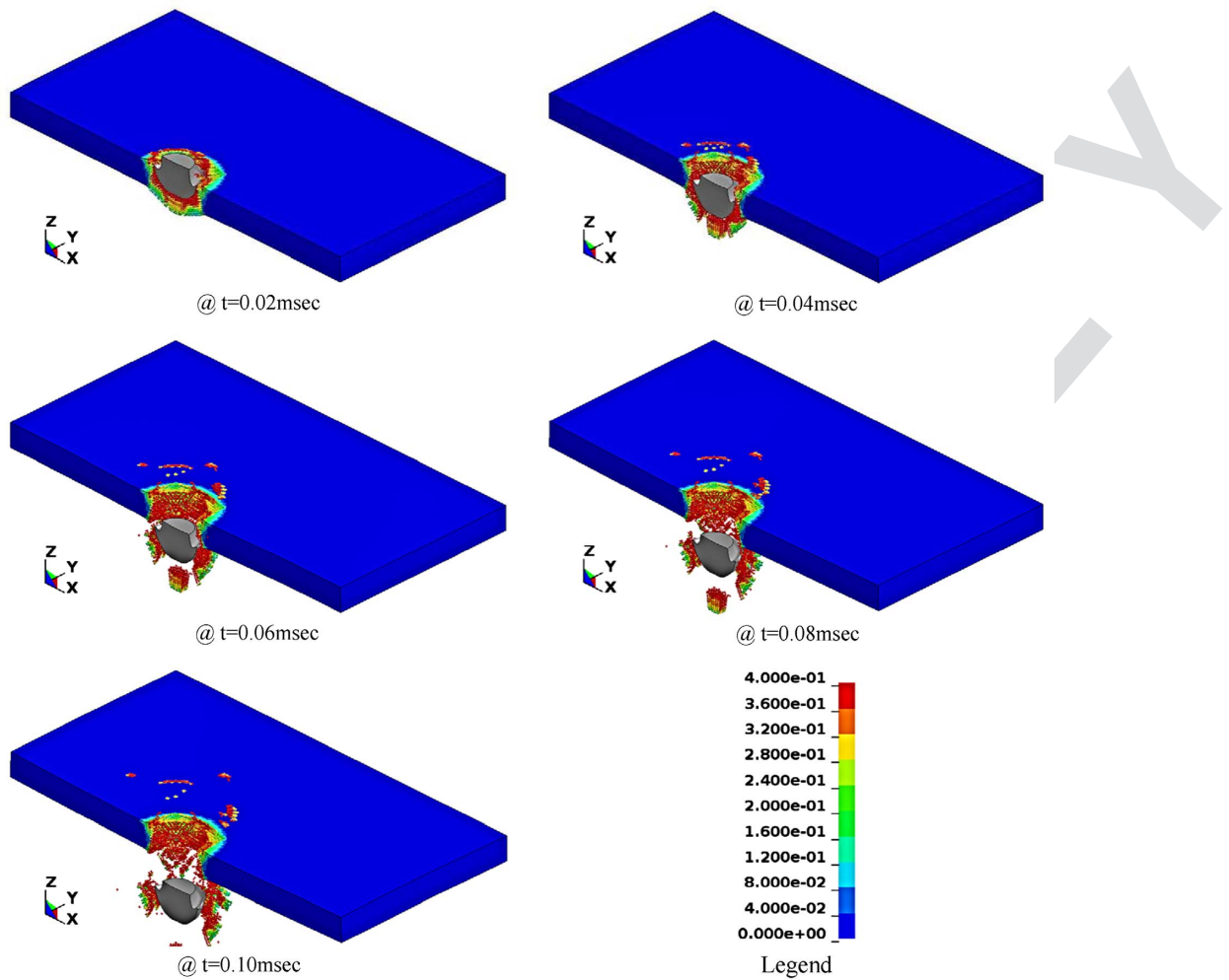
**Fig. 6.** Plate perforation: evolution of effective plastic strain.
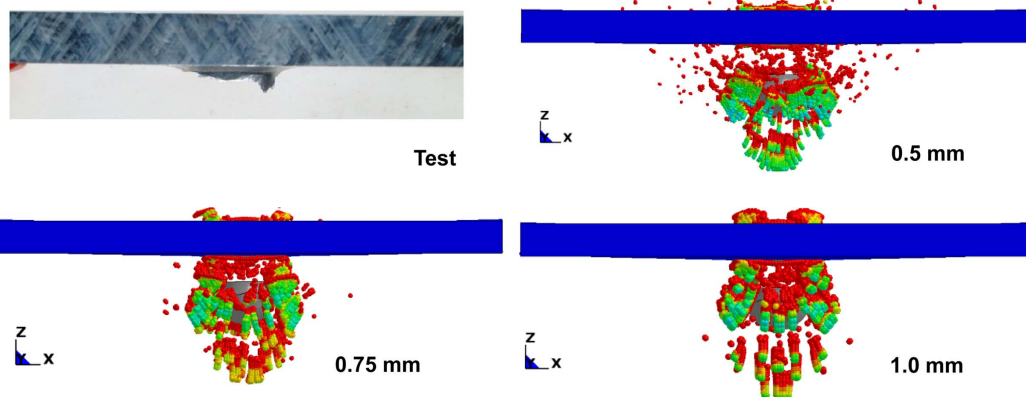
Fig. 7. Plate perforation: perforated plate, side view.

Fig. 12 shows the projectile velocity histories obtained using the FEM formulation with element erosion at effective plastic strains of 0.4 and 0.2 for the discretization shown in Fig. 3(c). The difference between the numerical solution and the experimental data increased from 20 to 40% when the effective plastic strain for element erosion decreased from 0.4 to 0.2, which indicates 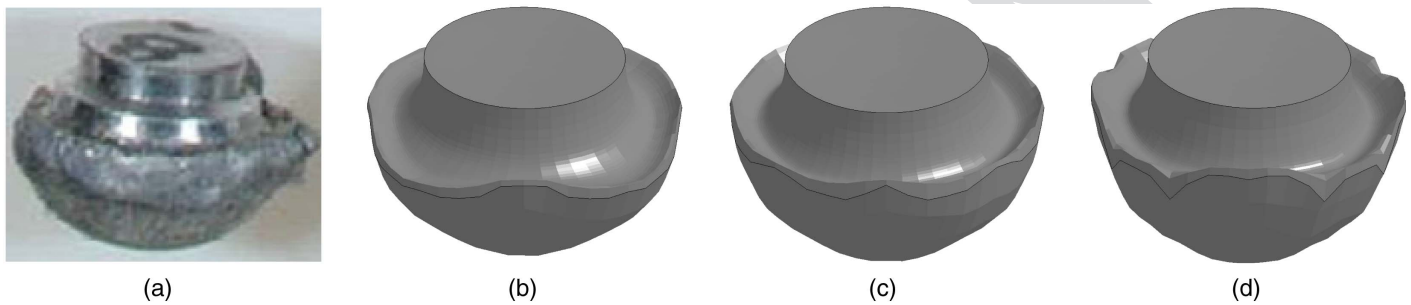that the FEM formulation has a serious failure criterion dependency and is substantially different from the SPG formulation.
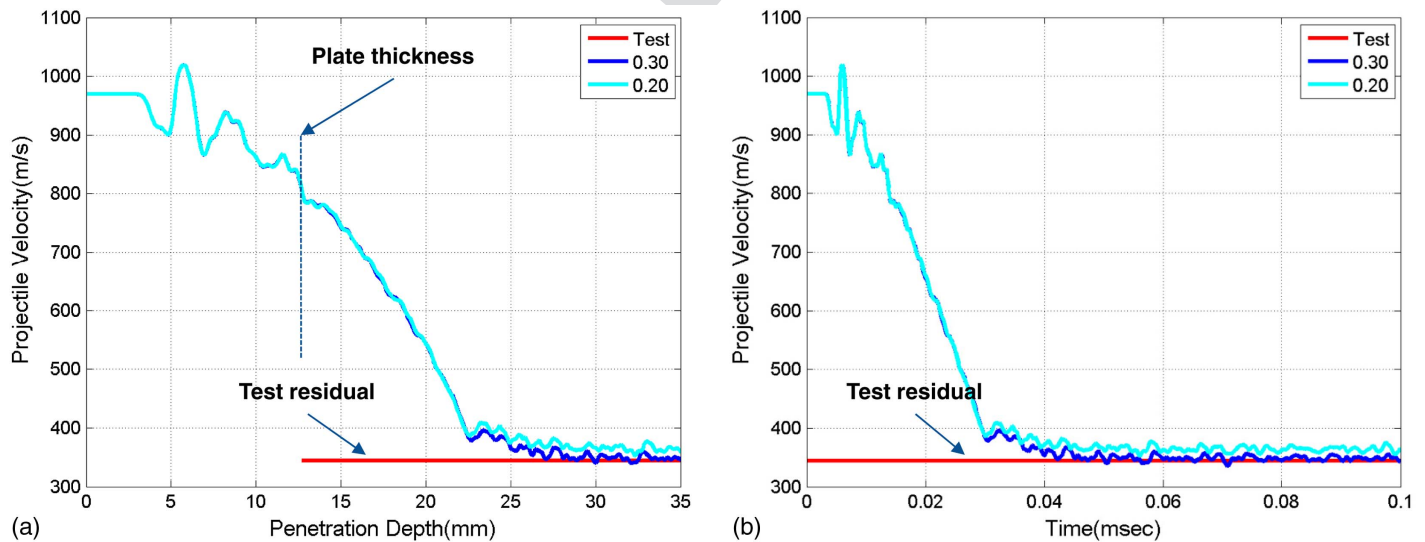
Effect of SPG Zone Size

The previous SPG solutions were obtained using the discretization in Fig. 3(c) or 13(a), in which only a central area of

7
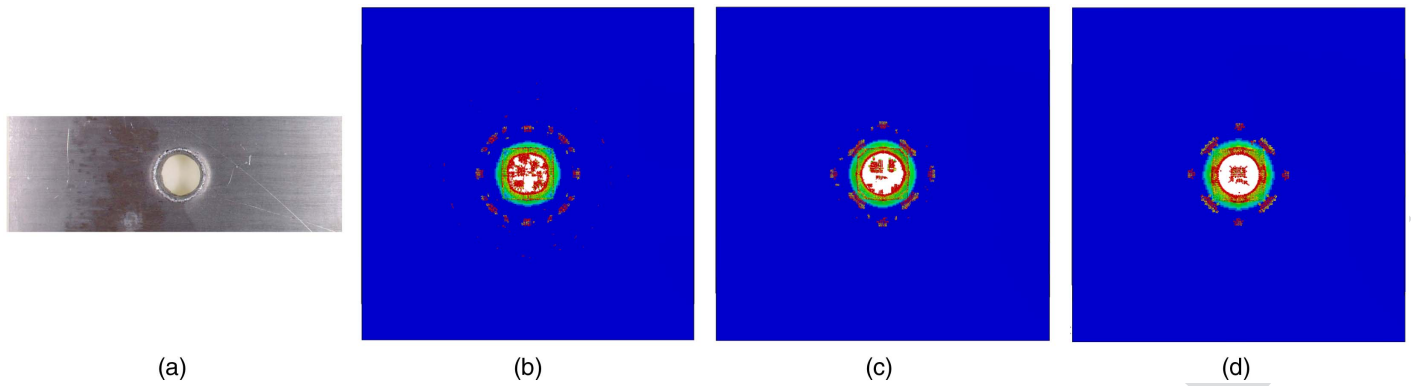
Fig. 8. Perforated plate for various discretizations: (a) test; (b) 0.5 mm; (c) 0.75 mm; and (d) 1.0 mm.

Fig. 9. Deformed projectile for various discretizations: (a) test; (b) 0.5 mm; (c) 0.75 mm; and (d) 1.0 mm.

Fig. 10. Plate perforation: sensitivity to coefficient of friction.

30×30 mm was modeled by SPG. To study whether or not this SPG domain was large enough to properly capture the impact phenomena, another discretization [Fig. 13(b)] discretized a central area of 60×60 mm.

Fig. 14 shows the projectile velocity histories obtained using the SPG formulation with the discretizations in Fig. 13 for a bond failure criterion of $\varepsilon_{crit}^{p} = 0.4$. Nearly identical responses were obtained for the two discretizations, which indicates that the smaller SPG domain is good enough to capture the impact perforation responses in this case. Generally, an SPG domain that is just slightly larger than the region in which failure occurs is sufficient

for modeling the impact penetration and perforation responses of ductile metallic targets.

Penetration Response of Steel Structure

This section uses a tungsten rod impacting a flat rolled homogeneous armor (RHA) steel target (Rajendran 1998) to investigate the capability of the proposed formulations in modeling penetration response. The tested RHA steel cylindrical target had a diameter of 100 mm and a thickness of 127 mm (Fig. 15). The penetrator rod had a diameter of 7.87 mm and a length of 78.74 mm and was made

© ASCE ·

8 · J. Eng. Mech.
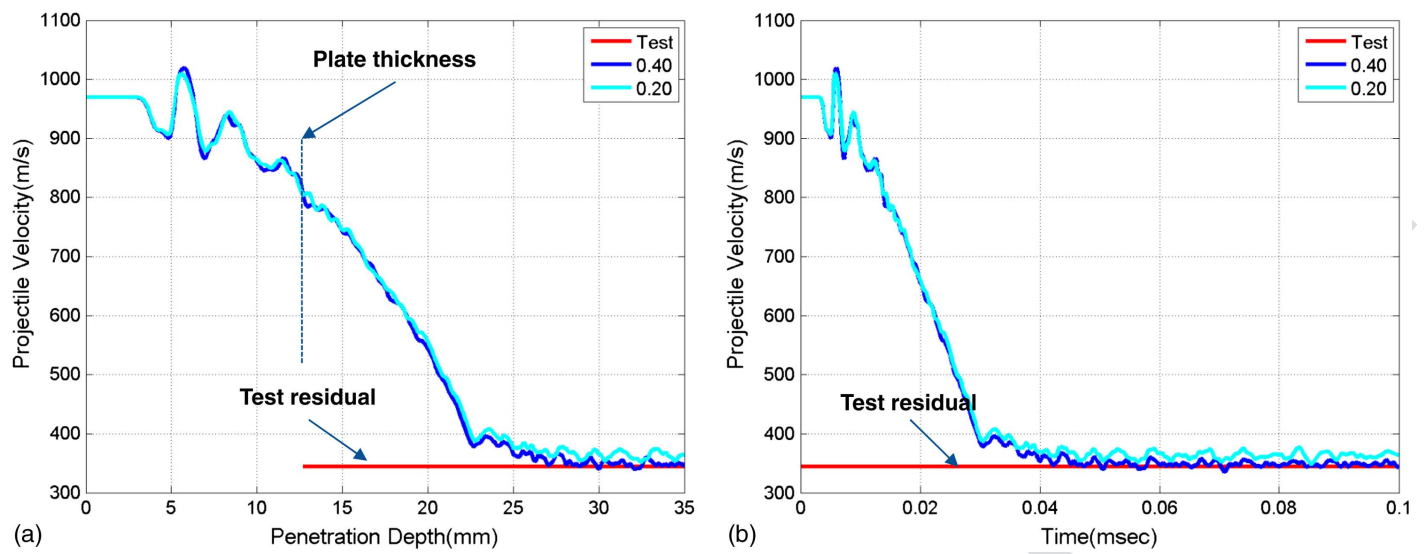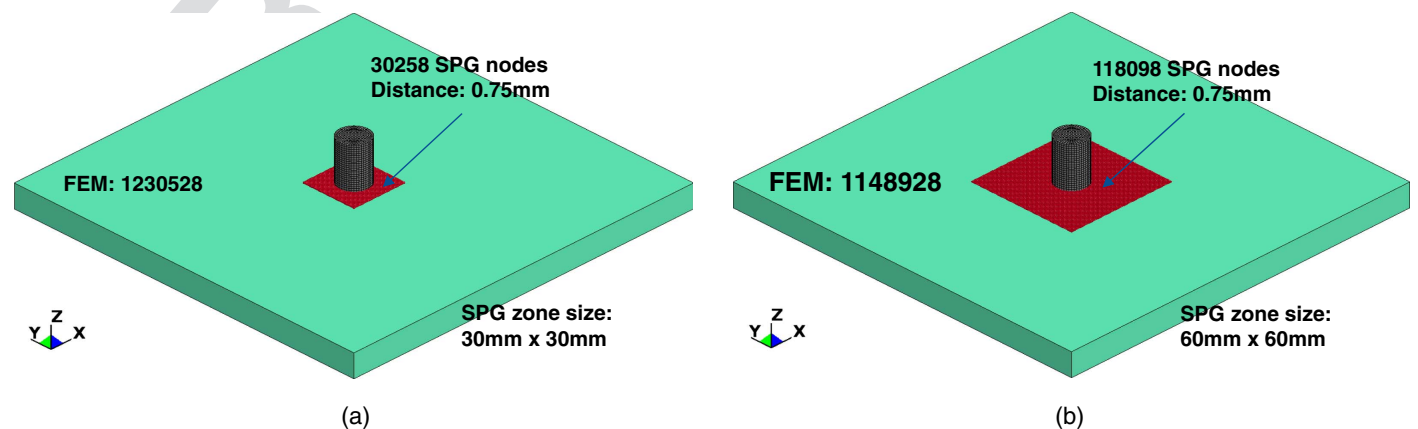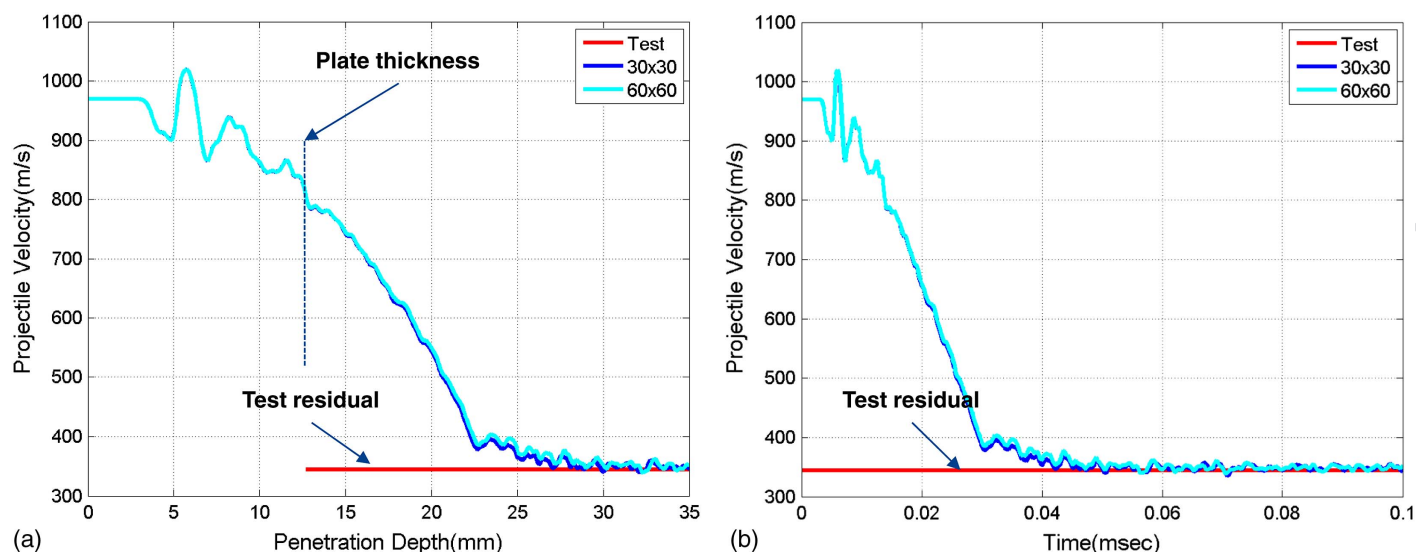
Fig. 11. Plate perforation: various failure criteria, SPG solution.
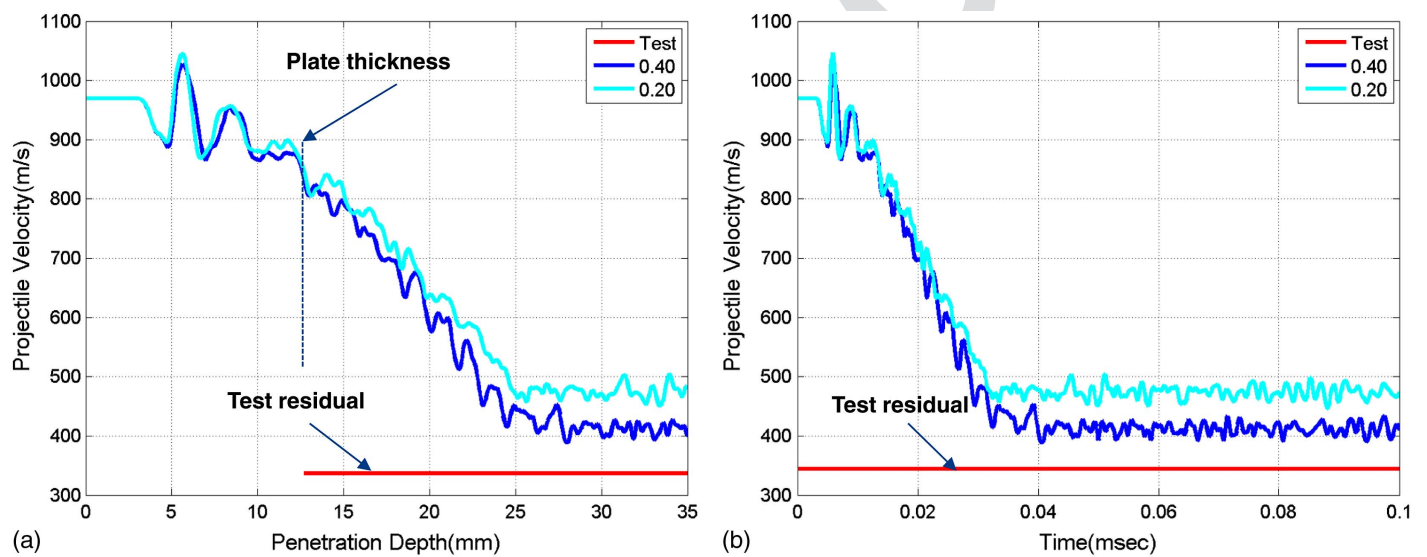
Fig. 12. Plate perforation: various failure criteria, FEM solution.

Fig. 13. Plate perforation: SPG zone size effect (discretizations).

F14:1 **Fig. 14.** Plate perforation: solutions from various discretizations.

from tungsten alloy. The penetrator impacted the target at a velocity
of 1,500 m/s normal to the center of the cylinder.

To reduce the computational cost, only the central area (diameter of 12 mm) of the target was modeled by the proposed SPG
formulation, whereas the majority of the target was modeled using
FEM because no failure occurred in that region and the interface
between FEM and SPG did not interfere with the dynamic wave
propagation (Wu et al. 2017a). The target was discretized by
282,240 finite elements and 56,953 SPG nodes with a nodal

F15:1 **Fig. 15.** Penetration response: problem statement.

distance of around 0.68 mm (Fig. 16). The perimeter of the target
was fixed. The penetrator was discretized by 42,752 finite elements. Because the aspect ratio of the penetrator was 10:1 (length
to diameter), to facilitate the numerical simulation, the penetrator
was treated as elastic with a Young's modulus of 327 GPa. The
friction coefficient between the penetrator and the target was 0.50
(www.engineeringtoolbox.com). The average DOP from the experiments was 69.6 mm. The target material was constitutively
modeled by the Johnson–Cook model with the exact parameters
used by Rajendran (1998). Effective plastic strain was used as the
indicator for SPG bond failure. To study the sensitivity of the penetration response to the bond failure criterion, four criteria were
used, i.e., $\varepsilon_{crit}^p = 0.30$ (FS = 0.30), $\varepsilon_{crit}^p = 0.45$ (FS = 0.45), $\varepsilon_{crit}^p = 0.90$ (FS = 0.90), and $\varepsilon_{crit}^p = 1.50$ (FS = 1.50). Failure criteria
FS = 0.30 and 0.45 are usually considered for high-strength and
regular-strength steel, and Rajendran (1998) used FS = 1.50 for
the Elastic-Plastic Impact Computations (EPIC) code (Johnson and
Stryk 1986) which used FEM with erosion.

Fig. 17 presents the velocity history and the DOP of the penetrator. The legend shows the critical effective plastic strain (FS)
for SPG bond failure. Fig. 17(a) indicates that the penetrator velocity reversed (to negative) and then quickly approached zero, which
means that the penetrator stayed in the target and the response was
penetration. Fig. 17(b) reveals that the DOP matched the experimental data well. The difference between the numerical solutions
and the experimental data was less than 2% for all cases. The results
were not sensitive to the bond failure criteria. This insensitivity to
the bond failure criteria was not surprising because the SPG bond
failure only occurred in the excessively high-strain area limited by
the contact zone between the impactor and metal target.

Figs. 18 and 19 demonstrate the effective plastic strain and von
Mises stress, respectively, at termination for various bond failure
criteria on the section cut view. Negligible difference was observed
between the different cases, which explains the similarity between
the DOPs and indicates the insensitivity to the bond failure criteria
in the SPG simulation of impact penetration on metal targets.
As mentioned in the "Mechanism for Severe Deformation and
Material Failure" section, the state variables (i.e., stress and strain)
continue to evolve according to the constitutive model after a bond
failure because the particle might be covered by other particles.
This explains how the effective plastic strain at termination for the
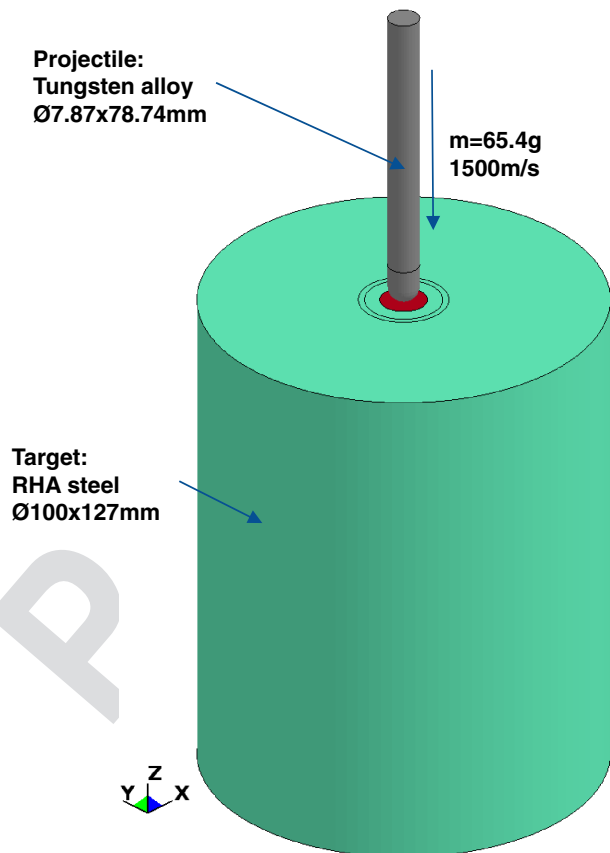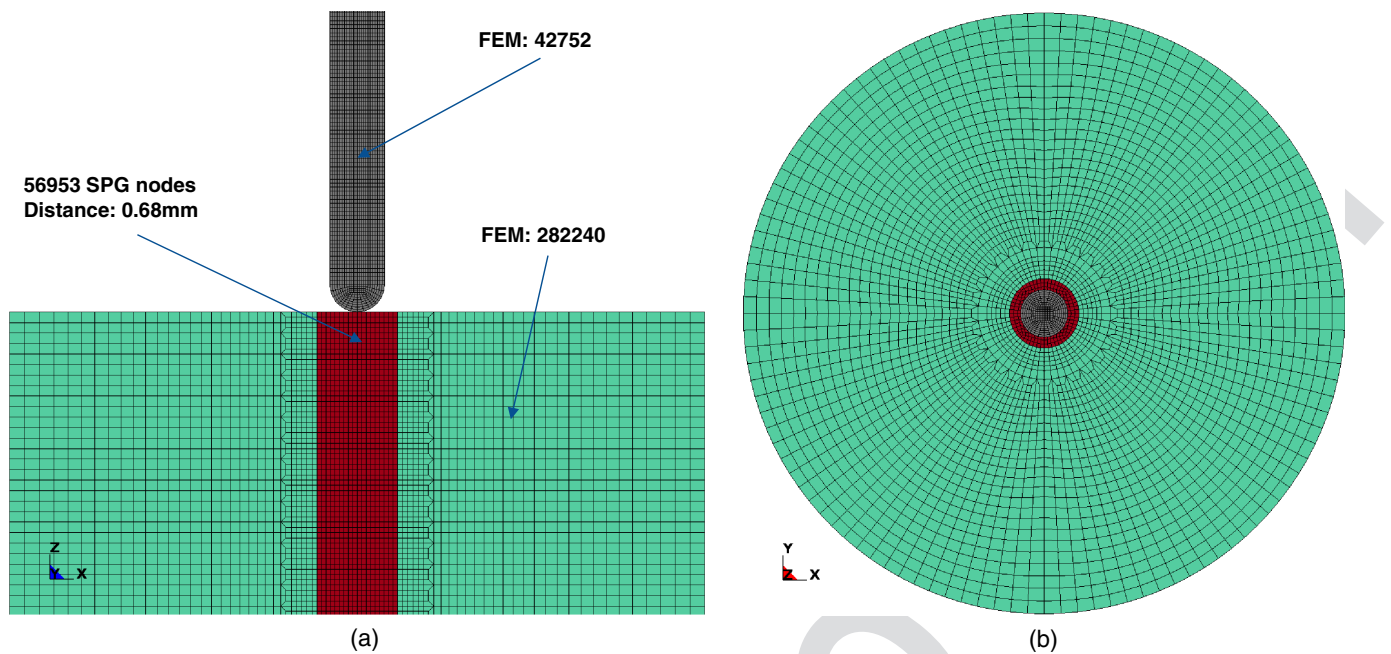
Fig. 16. Penetration geometry discretization: (a) cut through midplane; and (b) cross-section view.
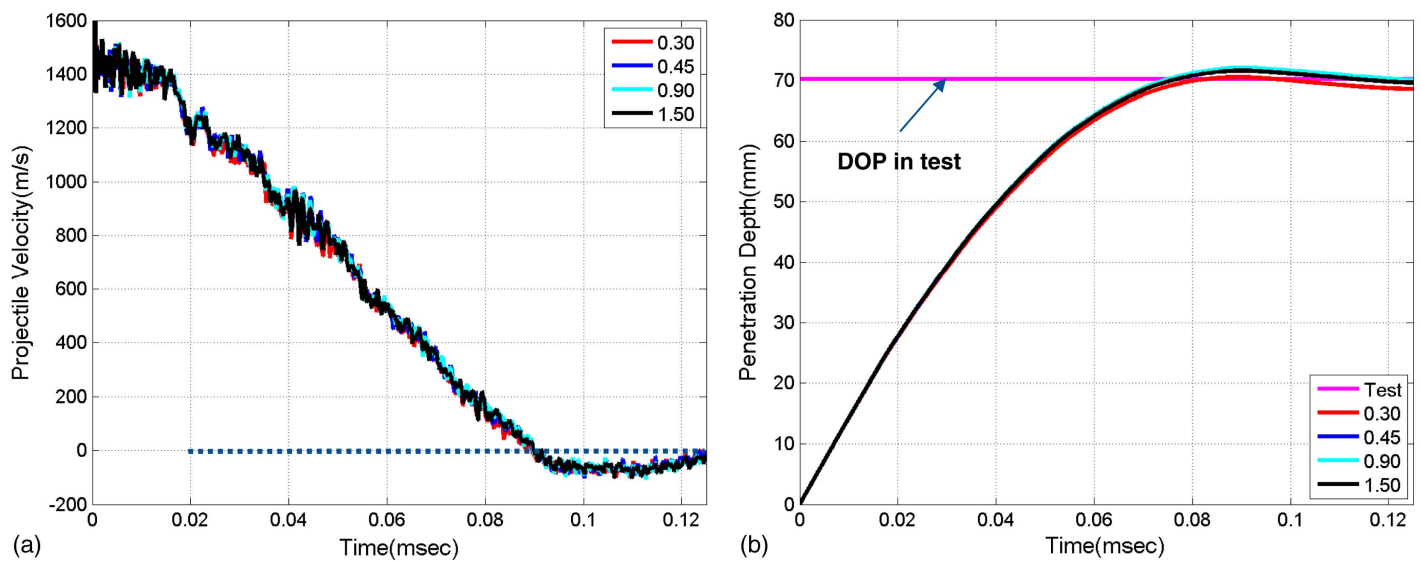
Fig. 17. Penetration response: (a) penetrator velocity history; and (b) penetration depth history.

506 FS = 0.30, 0.45, and 0.90 cases can still reach 1.5 or more under
507 the compression state. Because of this similarity of effective plastic
508 strain distribution, very close stress distribution was observed as
509 well for all the cases.

510 Figs. 20 and 21 illustrate the evolution of effective plastic strain
511 and von Mises stress, respectively, for the case of FS = 0.45 on the
512 section cut view. The material damage (i.e., high effective plastic
513 strain area) was very localized, which is typical in penetration
514 response. A very intense stress wave was generated by the impact
515 contact and it propagated as the tungsten alloy rod penetrated into
516 the RHA steel target. A rarefaction wave was also observed as the
517 penetrator reached the peak DOP and rebounded (at t = 0.125 ms).
518 Generally speaking, the impact wave propagation was reasonably
519 captured by the SPG formulation.

Conclusions

520

521 Impact penetration and perforation are characterized by large strain
522 and high strain rates, large amounts of material failure and sepa-
523 ration, high-frequency stress waves, and complex contact condi-
524 tions. These features impose challenges for numerical prediction of
525 the impact responses. This paper introduced the smoothed particle
526 Galerkin (SPG) formulation to analyze the impact response of
527 metal targets. A nonresidual-type penalty term derived from strain
528 smoothing was used for stabilization under the direct nodal integra-
529 tion framework so that the algorithm is efficient and stable. Mean-
530 while, to deal with large deformation in the impact region, the
531 meshfree approximation used an adaptive anisotropic Lagrangian
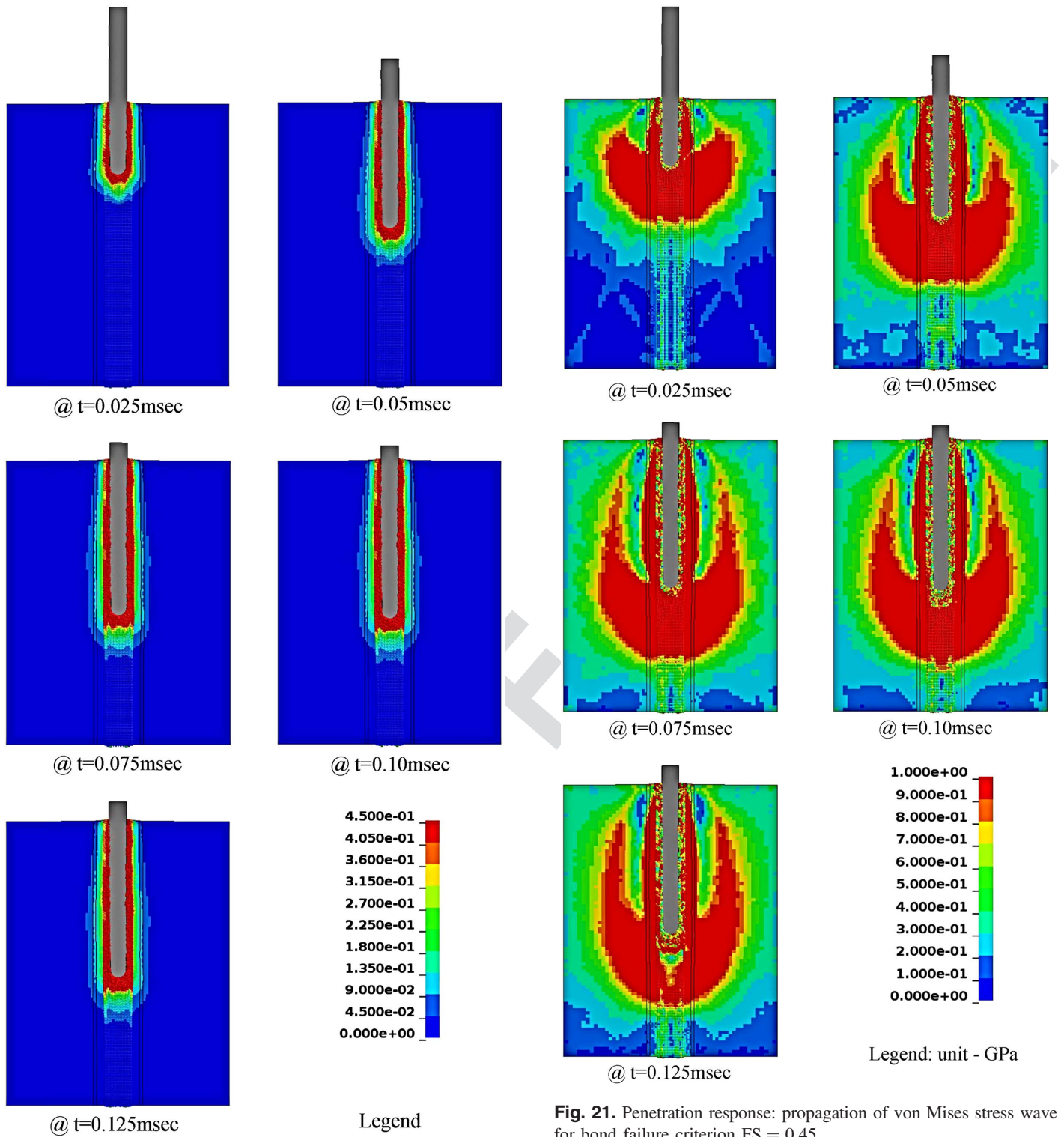532 kernel. To allow material failure (crack initiation) and separation
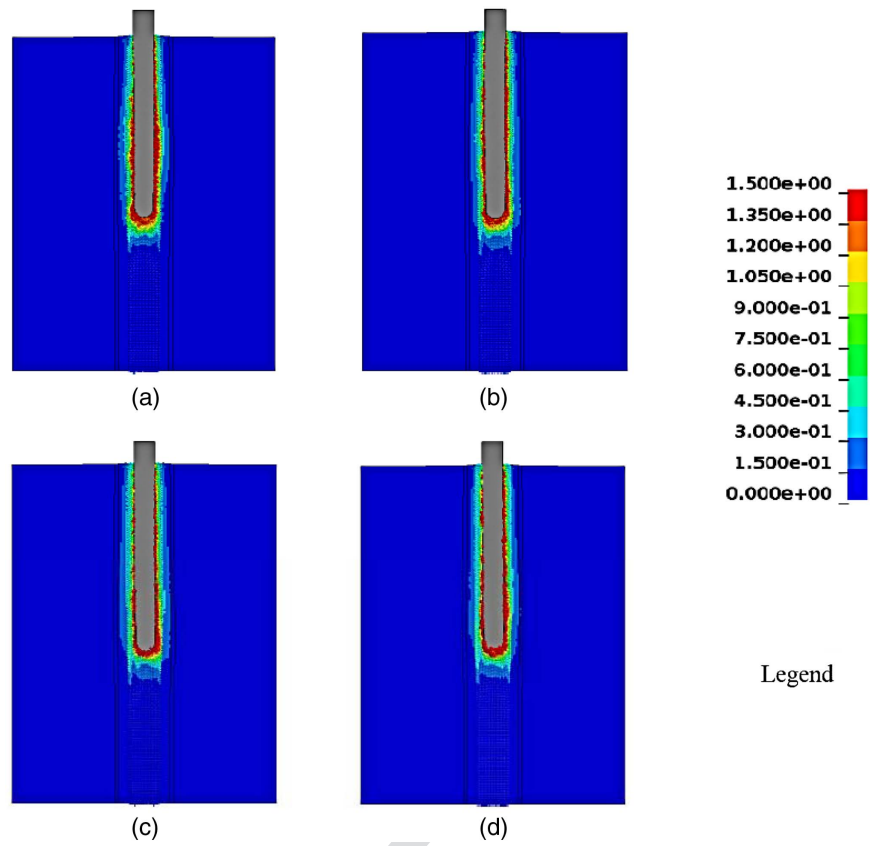
F18:1 **Fig. 18.** Penetration response: effective plastic strain at termination for various bond failure criteria: (a) FS = 0.30; (b) FS = 0.45; (c) FS = 0.90; and
F18:2 (d) FS = 1.50.
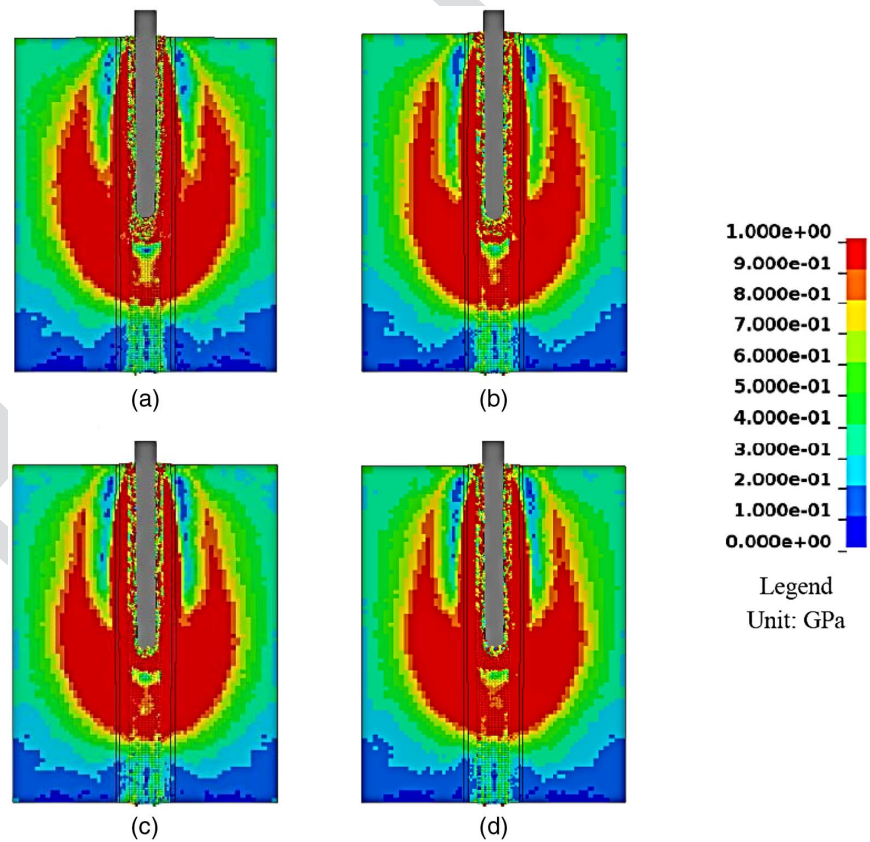
F19:1 **Fig. 19.** Penetration response: von Mises stress distribution at termination for various bond failure criteria: (a) FS = 0.30; (b) FS = 0.45;
F19:2 (c) FS = 0.90; and (d) FS = 1.50.

@ t=0.025msec @ t=0.05msec

@ t=0.075msec @ t=0.10msec

@ t=0.125msec

4.500e-01
4.050e-01
3.600e-01
3.150e-01
2.700e-01
2.250e-01
1.800e-01
1.350e-01
9.000e-02
4.500e-02
0.000e+00

Legend

Fig. 20. Penetration response: evolution of effective plastic strain for bond failure criterion FS = 0.45.

@ t=0.025msec @ t=0.05msec

@ t=0.075msec @ t=0.10msec

1.000e+00
9.000e-01
8.000e-01
7.000e-01
6.000e-01
5.000e-01
4.000e-01
3.000e-01
2.000e-01
1.000e-01
0.000e+00

Legend: unit - GPa

@ t=0.125msec

Fig. 21. Penetration response: propagation of von Mises stress wave for bond failure criterion FS = 0.45.

(crack propagation) while avoiding spurious self-healing issues in numerical failure analysis of metals, a strain-based bond failure mechanism was introduced to initiate and propagate cracks in metal materials with self-contact being defined between the failed particles.

The numerical results showed the potential of the present formulations in application to analysis of high velocity impact in metal targets. In general, stable and accurate results were obtained for the perforation and penetration responses analyzed. First, no discretization sensitivity was observed provided that the discretization was fine enough to propagate the high-frequency stress waves generated by impact contact. Second, no failure criterion sensitivity was observed, which makes it much easier to set up a simulation. This is in sharp contrast to the ad hoc erosion criterion for the traditional FEM with element erosion technique for this type of analysis.

Although the current formulation treated the failure and fragmentation of the target, more research still needs to be done in the analysis of impact phenomena. For example, the contact conditions

in hypervelocity impact are complicated because both the impactor and target can be deformed severely and even fragmented, which is a challenge for traditional contact algorithms with contact surfaces defined a priori. The material constitutive modeling, especially for the impactor, is another issue in high-velocity and hypervelocity impact, not only because of the high strain rates but also because of the size effect. Further developments of such analyses will be discussed and presented in the future.

Acknowledgments

References

Asadi Kalameh, H., A. Karamali, C. Anitescu, and T. Rabczuk. 2012. "High velocity impact of metal sphere on thin metallic plate using smooth particle hydrodynamics." *Front. Struct. Civ. Eng.* 6 (2): 101–110.

Belytschko, T., Y. Guo, W. K. Liu, and S. P. Xiao. 2000. "A unified stability analysis of meshless particle methods." *Int. J. Numer. Methods Eng.* 48 (9): 1359–1400. https://doi.org/10.1002/1097-0207(20000730)48:9<1359::AID-NME829>3.0.CO;2-U.

Belytschko, T., and A. Lin. 1987. "A three-dimensional impact-penetration algorithm with erosion." *Int. J. Impact Eng.* 5 (1–4): 111–127. https://doi.org/10.1016/0734-743X(87)90033-9.

Belytschko, T., Y. Y. Lu, and L. Gu. 1994. "Element-free Galerkin methods." *Int. J. Numer. Methods Eng.* 37 (2): 229–256. https://doi.org/10.1002/nme.1620370205.

Ben-Dor, G., A. Dubinsky, and T. Elperin. 2005. "Ballistic impact: Recent advances in analytical modeling of plate penetration dynamics–A review." *Appl. Mech. Rev.* 58 (6): 355–371. https://doi.org/10.1115/1.2048626.

Bishop, R. F., R. Hill, and N. F. Mott. 1945. "The theory of indentation and hardness tests." *Proc. Phys. Soc.* 57 (3): 147–159. https://doi.org/10.1088/0959-5309/57/3/301.

Chandel, P. S., D. Sood, R. Kumar, P. Sharma, B. Sewak, V. Bhardwaj, M. Athwal, V. Mangla, I. Biswas, and M. Singh. 2012. "Hypervelocity impact of tungsten cubes on spaced armour." *J. Phys. Conf. Ser.* 377: 012048. https://doi.org/10.1088/1742-6596/377/1/012048.

Chen, J. S., M. Hillman, and M. Ruter. 2013. "An arbitrary order variationally consistent integration for Galerkin meshfree methods." *Int. J. Numer. Methods Eng.* 95 (5): 387–418. https://doi.org/10.1002/nme.4512.

Chen, J. S., C. Pan, C. T. Wu, and W. K. Liu. 1996. "Reproducing kernel particle methods for large deformation analysis of non-linear structures." *Comput. Methods Appl. Mech. Eng.* 139 (1–4): 195–227. https://doi.org/10.1016/S0045-7825(96)01083-3.

Chen, J. S., C. T. Wu, S. Yoon, and Y. You. 2001. "A stabilized conforming nodal integration for Galerkin meshfree methods." *Int. J. Numer. Methods Eng.* 50 (2): 435–466. https://doi.org/10.1002/1097-0207(20010120)50:2<435::AID-NME32>3.0.CO;2-A.

Dikshit, S. N., and G. Sundararajan. 1992. "The penetration of thick steel plates by ogive shaped projectiles–experiment and analysis." *Int. J. Impact Eng.* 12 (3): 373–408. https://doi.org/10.1016/0734-743X(92)90134-F.

Fahrenthold, E. P., and B. A. Horban. 2001. "An improved hybrid particle-element method for hypervelocity impact simulation." *Int. J. Impact Eng.* 26 (1–10): 169–178. https://doi.org/10.1016/S0734-743X(01)00079-3.

Forrestal, M. J., and V. K. Luk. 1992. "Penetration into soil targets." *Int. J. Impact Eng.* 12 (3): 427–444. https://doi.org/10.1016/0734-743X(92)90167-R.

Forrestal, M. J., D. Y. Tzou, E. Askari, and D. B. Longcope. 1995. "Penetration into ductile metal targets with rigid spherical-nose rods." *Int. J. Impact Eng.* 16 (5–6): 699–710. https://doi.org/10.1016/0734-743X(95)00005-U.

Fountzoulas, C. G., G. A. Gazonas, and B. A. Cheeseman. 2007. "Computational modeling of tungsten carbide sphere impact and penetration into high-strength-low-alloy (HSLA)-100 steel targets." *J. Mech. Mater. Struct.* 2 (10): 1965–1979. https://doi.org/10.2140/jomms.2007.2.1965.

Gingold, R. A., and J. J. Monaghan. 1977. "Smooth particle hydrodynamics: Theory and application to non-spherical stars." *Mon. Not. R. Astron. Soc.* 181 (3): 375–389. https://doi.org/10.1093/mnras/181.3.375.

Golsdmith, W., and S. A. Finnegan. 1971. "Penetration and perforation processes in metal targets at and above ballistic velocities." *Int. J. Mech. Sci.* 13 (10): 843–866. https://doi.org/10.1016/0020-7403(71)90111-1.

Goodier, J. N. 1964. *On the mechanics of indentation and cratering in solid targets of strain-hardening metal by impact of hard and soft spheres.* Menlo Park, CA: Stanford Research Institute.

Guan, P. C., J. S. Chen, Y. Wu, H. Teng, J. Gaidos, K. Hofstetter, and M. Alsaleh. 2009. "Semi-Lagrangian reproducing kernel formulation and application to modeling earth moving operations." *Mech. Mater.* 41 (6): 670–683. https://doi.org/10.1016/j.mechmat.2009.01.030.

Hallquist, J. O. 2006. *LS-DYNA keyword user's manual.* Livermore, CA: Livermore Software Technology.

Hohler, V., A. Stilp, and K. Weber. 1995. "Hypervelocity penetration of tungsten sinter-alloy rods into aluminum." *Int. J. Impact Eng.* 17 (1–3): 409–418. https://doi.org/10.1016/0734-743X(95)99866-P.

Huang, P., X. Zhang, S. Ma, and X. Huang. 2011. "Contact algorithms for the material point method in impact and penetration simulation." *Int. J. Numer. Methods Eng.* 85 (4): 498–517. https://doi.org/10.1002/nme.2981.

Ibne Islam, M. R., S. Chakraborty, A. Shaw, and S. Reid. 2017. "A computational model for failure of ductile material under impact." *Int. J. Impact Eng.* 108: 334–347. https://doi.org/10.1016/j.ijimpeng.2017.04.005.

Johnson, G. R., and W. H. Cook. 1983. "A constitutive model and data for metals subjected to large strains, high strain rates, and high temperatures." *Proc., 7th Int. Symp. on Ballistics*, 541–547. The Hague, Netherlands.

Johnson, G. R., and R. A. Stryk. 1986. *User instructions for the EPIC-2 code.* AFATL-TR-86-51. Eglin Air Force Base, FL.

Johnson, G. R., and R. A. Stryk. 1987. "Eroding interface and improved tetrahedral element algorithms for high-velocity impact computations in three dimensions." *Int. J. Impact Eng.* 5 (1–4): 411–421. https://doi.org/10.1016/0734-743X(87)90057-1.

Lacerda, D., and J. L. Lacome. 2001. "Simulations of hypervelocity impacts with smoothed particle hydrodynamics." *3rd European LSYDNA Conf*. Paris, France.

Li, Q. M., and X. W. Chen. 2003. "Dimensionless formulae for penetration depth of concrete target impacted by a non-deformable projectile." *Int. J. Impact Eng.* 28 (1): 93–116. https://doi.org/10.1016/S0734-743X(02)00037-4.

Li, S., and W. K. Liu. 2004. *Meshfree particle method.* Berlin: Springer.

Liden, E., S. Mousavi, A. Helte, and B. Lundberg. 2012. "Deformation and fracture of a long-rod projectile induced by an oblique moving plate: Numerical simulations." *Int. J. Impact Eng.* 40–41: 35–45. https://doi.org/10.1016/j.ijimpeng.2011.09.003.

Liu, G. R., K. Y. Dai, and T. T. Nguyen. 2007. "A smoothed finite element method for mechanics problems." *Comput. Mech.* 39 (6): 859–877. https://doi.org/10.1007/s00466-006-0075-4.

Liu, W. K., S. Jun, and Y. F. Zhang. 1995. "Reproducing kernel particle methods." *Int. J. Numer. Methods Fluids* 20 (8–9): 1081–1106. https://doi.org/10.1002/fld.1650200824.

Lu, Z. C., and H. M. Wen. 2018. "On the penetration of high strength steel rods into semi-infinite aluminum alloy targets." *Int. J. Impact Eng.* 111: 1–10. https://doi.org/10.1016/j.ijimpeng.2017.08.006.

Lucy, L. B. 1977. "A numerical approach to the testing of the fission hypothesis." *Astron. J.* 82 (12): 1013–1024. https://doi.org/10.1086/112164.

Mohotti, D., S. N. Raman, T. Ngo, and P. Mendis. 2015. "Use of coupled smooth-particle hydrodynamics/Lagrangian method in the simulation of deformable projectile penetration." *Int. J. Protective Struct.* 6 (3): 419–437. https://doi.org/10.1260/2041-4196.6.3.419.

Nechitailo, N. 2015. "Hypervelocity penetration into soil." *Procedia Eng.* 103: 427–435. https://doi.org/10.1016/j.proeng.2015.04.042.

Nguyen-Xuan, H., T. Rabczuk, S. P. A. Bordas, and J. F. Debongnie. 2008. "A smoothed finite element method for plate analysis." *Comput. Methods Appl. Mech. Eng.* 197 (13–16): 1184–1203. https://doi.org/10.1016/j.cma.2007.10.008.

Orphal, D. L., and R. R. Franzen. 1997. "Penetration of confined silicon carbide targets by tungsten long rods at impact velocities from 1.5 to 4.6 km/s." *Int. J. Impact Eng.* 19 (1): 1–13. https://doi.org/10.1016/0734-743X(95)00064-H.

Orphal, D. L., R. R. Franzen, A. C. Charters, T. L. Menna, and A. J. Piekutowski. 1997. "Penetration of confined boron carbide targets by tungsten long rods at impact velocities from 1.5 to 5.0 km/s." *Int. J. Impact Eng.* 19 (1): 15–29. https://doi.org/10.1016/S0734-743X(96)00004-8.

Park, C. K., C. T. Wu, and C. D. Kan. 2011. "On the analysis of dispersion property and stable time step in meshfree method using the generalized meshfree approximation." *Finite Elem. Anal. Des.* 47 (7): 683–697. https://doi.org/10.1016/j.finel.2011.02.001.

Pedersen, B., and S. Bless. 2006. "Behind-armor debris from the impact of hypervelocity tungsten penetrators." *Int. J. Impact Eng.* 33 (1–12): 605–614. https://doi.org/10.1016/j.ijimpeng.2006.09.007.

Plassard, F., J. Mespoulet, and P. Hereil. 2011. "Hypervelocity impact of aluminum sphere against aluminum plate: Experiment and LS-DYNA correlation." *8th European LS-DYNA Conf.* Strasbourg, France.

Puso, M. A., J. S. Chen, E. Zywicz, and W. Elmer. 2008. "Meshfree and finite element nodal integration methods." *Int. J. Numer. Methods Eng.* 74 (3): 416–446. https://doi.org/10.1002/nme.2181.

Rabczuk, T., T. Belytschko, and S. P. Xiao. 2004. "Stable particle methods based on Lagrangian kernels." *Comput. Methods Appl. Mech. Eng.* 193 (12–14): 1035–1063. https://doi.org/10.1016/j.cma.2003.12.005.

Rajendran, A. M. 1998. "Penetration of tungsten alloy rods into shallow—Cavity steel targets." *Int. J. Impact Eng.* 21 (6): 451–460. https://doi.org/10.1016/S0734-743X(98)00005-0.

Randles, P. W., T. C. Carney, L. D. Libersky, J. D. Renick, and A. G. Petschek. 1995. "Calculation of oblique impact and fracture of tungsten cubes using smoothed particle hydrodynamics." *Int. J. Impact Eng.* 17 (4–6): 661–672. https://doi.org/10.1016/0734-743X(95)99889-Y.

Roy, S. K., et al. 2016. "Study of hypervelocity projectile impact on thick metal plates." *Shock Vibr.* https://doi.org/10.1155/2016/4313480.

Sataphathy, S. 2001. "Dynamic spherical cavity expansion in brittle ceramics." *Int. J. Solids Struct.* 38 (32–33): 5833–5845. https://doi.org/10.1016/S0020-7683(00)00388-7.

Schwer, L. E. 2009. "Aluminum plate perforation: A comparative case study using Lagrange with erosion, multi-material ALE, and smooth particle hydrodynamics." *7th European LS-DYNA Conf.* Salzburg, Austria.

Sherburn, J. A., M. J. Roth, J. S. Chen, and M. Hillman. 2015. "Meshfree modeling of concrete slab perforation using a reproducing kernel particle impact and penetration formulation." *Int. J. Impact Eng.* 86: 96–110. https://doi.org/10.1016/j.ijimpeng.2015.07.009.

Silling, S. A., and E. Askari. 2005. "A meshfree method based on the peridynamic model of solid mechanics." *Comput. Struct.* 83 (17–18): 1526–1535. https://doi.org/10.1016/j.compstruc.2004.11.026.

Simkins, D. C., and S. Li. 2006. "Meshfree simulation of thermo-mechanical ductile fracture." *Comput. Mech.* 38 (3): 235–249. https://doi.org/10.1007/s00466-005-0744-8.

Simo, J. C., and T. J. R. Hughes. 1986. "On the variational foundations of assumed strain methods." *J. Appl. Mech.* 53 (1): 51–54. https://doi.org/10.1115/1.3171737.

Sorensen, B. R., K. D. Kimsey, G. F. Silsby, D. R. Scheffler, T. M. Sherrick, and W. S. Rosset. 1991. "High velocity penetration of steel targets." *Int. J. Impact Eng.* 11 (1): 107–119. https://doi.org/10.1016/0734-743X(91)90034-D.

Violeau, D. 2012. *Fluid mechanics and the SPH method: Theory and applications.* Oxford: Oxford University Press.

Wang, D., and J. S. Chen. 2004. "Locking-free stabilized conforming nodal integration for meshfree Mindlin–Reissner plate formulation." *Comput. Methods Appl. Mech. Eng.* 193 (12–14): 1065–1083. https://doi.org/10.1016/j.cma.2003.12.006.

Wang, D., and J. S. Chen. 2006. "A locking-free meshfree curved beam formulation with the stabilized conforming nodal integration." *Comput. Mech.* 39 (1): 83–90. https://doi.org/10.1007/s00466-005-0010-0.

Wang, D., and Z. Li. 2013. "A two-level strain smoothing regularized meshfree approach with stabilized conforming nodal integration for elastic damage analysis." *Int. J. Damage Mech.* 22 (3): 440–459. https://doi.org/10.1177/1056789512455938.

Wang, D., and H. Peng. 2013. "A Hermite reproducing kernel Galerkin meshfree for buckling analysis of thin plates." *Comput. Mech.* 51 (6): 1013–1029. https://doi.org/10.1007/s00466-012-0784-9.

Watson, E., and M. O. Steinhauser. 2017. "Discrete particle method for simulating hypervelocity impact phenomena." *Materials* 10 (12): 379. https://doi.org/10.3390/ma10040379.

Wu, C. T., T. Q. Bui, Y. Wu, T. L. Luo, M. Wang, C. C. Liao, P. Y. Chen, and Y. S. Lai. 2017a. "Numerical and experimental validation of a particle Galerkin method for metal grinding simulation." *Comput. Mech.* https://doi.org/10.1007/s00466-017-1456-6.

Wu, C. T., S. W. Chi, M. Koishi, and Y. Wu. 2016a. "Strain gradient stabilization with dual stress points for the meshfree nodal integration method in inelastic analysis." *Int. J. Numer. Methods Eng.* 107 (1): 3–30. https://doi.org/10.1002/nme.5147.

Wu, C. T., and M. Koishi. 2012. "Three-dimensional meshfree-enriched finite element formulation for micromechanical hyperelastic modeling of particulate rubber composites." *Int. J. Numer. Methods Eng.* 91 (11): 1137–1157. https://doi.org/10.1002/nme.4306.

Wu, C. T., M. Koishi, and W. Hu. 2015a. "A displacement smoothing induced strain gradient stabilization for the meshfree Galerkin nodal integration method." *Comput. Mech.* 56 (1): 19–37. https://doi.org/10.1007/s00466-015-1153-2.

Wu, C. T., N. Ma, K. Takada, and H. Okada. 2016b. "A meshfree continuous-discontinuous approach for the ductile fracture modeling in explicit dynamics analysis." *Comput. Mech.* 58 (3): 391–409. https://doi.org/10.1007/s00466-016-1299-6.

Wu, C. T., C. K. Park, and J. S. Chen. 2011. "A generalized approximation for the meshfree analysis of solids." *Int. J. Numer. Methods Eng.* 85 (6): 693–722. https://doi.org/10.1002/nme.2991.

Wu, C. T., and B. Ren. 2015. "A stabilized non-ordinary state-based peridynamics for the nonlocal ductile material failure analysis in metal machining process." *Comput. Methods Appl. Mech. Eng.* 291: 197–215. https://doi.org/10.1016/j.cma.2015.03.003.

Wu, C. T., Y. Wu, J. E. Crawford, and J. M. Magallanes. 2017b. "Three-dimensional concrete impact and penetration simulations using the smoothed particle Galerkin method." *Int. J. Impact Eng.* 106: 1–17. https://doi.org/10.1016/j.ijimpeng.2017.03.005.

Wu, C. T., Y. Wu, and M. Koishi. 2015b. "A strain-morphed nonlocal meshfree method for the regularized particle simulation of elastic-damage induced strain localization problems." *Comput. Mech.* 56 (6): 1039–1054. https://doi.org/10.1007/s00466-015-1217-3.

Wu, Y., J. M. Magallanes, and J. E. Crawford. 2014a. "Fragmentation and debris evolution modeled by a point-wise coupled reproducing kernel-finite element formulation." *Int. J. Damage Mech.* 23 (7): 1005–1034. https://doi.org/10.1177/1056789514520797.

Wu, Y., D. Wang, and C. T. Wu. 2014b. "Three dimensional fragment simulation of concrete structures with a nodally regularized meshfree method." *Theor. Appl. Fract. Mech.* 72: 89–99. https://doi.org/10.1016/j.tafmec.2014.04.006.

Wu, Y., D. Wang, C. T. Wu, and H. Zhang. 2016c. "A direct displacement smoothing meshfree particle formulation for impact failure modeling." *Int. J. Impact Eng.* 87: 169–185. https://doi.org/10.1016/j.ijimpeng.2015.03.013.

Xiao, Y. K., H. Wu, Q. Fang, W. Zhang, and X. Z. Kong. 2017. "Hemisphere nosed steel projectile high-speed penetration into aluminum target." *Mater. Des.* 133: 237–254. https://doi.org/10.1016/j.matdes.2017.08.002.

Zhang, X., K. Y. Sze, and S. Ma. 2006. "An explicit material point finite element method for hypervelocity impact." *Int. J. Numer. Methods Eng.* 66 (4): 689–706. https://doi.org/10.1002/nme.1579.

Queries

1. Please provide the ASCE Membership Grades for the authors who are members.

2. Please provide department name for all author affiliation footnote.

3. Please check the hierarchy of section heading levels.

4. [ASCE Open Access: Authors may choose to publish their papers through ASCE Open Access, making the paper freely available to all readers via the ASCE Library website. ASCE Open Access papers will be published under the Creative Commons-Attribution Only (CC-BY) License. The fee for this service is $1750, and must be paid prior to publication. If you indicate Yes, you will receive a follow-up message with payment instructions. If you indicate No, your paper will be published in the typical subscribed-access section of the Journal.]

5. The citation Wu et al. (2016) has been changed to Wu et al. (2016c) to match with the reference list throughout the article.

6. The citation (Li et al. 2003) mentioned in this sentence is not present in the References list. Please provide the full details and we will insert it in the References list and link it to this citation.

7. The citation Watson et al. (2017) has been changed to Watson and Steinhauser (2017) to match with the reference list.

8. The citation (Belytschko 1994) mentioned in this sentence is not present in the References list. Please provide the full details and we will insert it in the References list and link it to this citation.

9. ASCE style for math is to set all mathematical variables in italic font. Please check all math variables throughout the paper, both in equations and throughout the text, to ensure all conform to ASCE style.

10. ASCE style for fences in math is in the order $\{[()]\}$. Please check to ensure all math conforms to this ASCE style.

11. ASCE style for matrices, vectors, and tensors is to designate them either using bold regular font (e.g., $\mathbf{A}$) or lightface italic font in fences (e.g., $[A]$), but not both. Elements of matrices, components of vectors, and subscripts and superscripts are set in italic. Please check throughout the paper to ensure all matrices, vectors, and tensors conform to this ASCE style.

12. Please check all figures, figure citations, and figure captions to ensure they match and are in the correct order.

13. Your figures will not print in color. Mentions of color have been edited out as shown. Please check and confirm.

14. Your figures will not print in color. Mentions of color have been edited out as shown. Please check and confirm.

15. As per ASCE style, URL not allowed in text throughout the article. Hence please move to the reference list and provide complete details.

16. This query was generated by an automatic reference checking system. This reference Asadi Kalameh et al. 2012 could not be located in the databases used by the system. While the reference may be correct, we ask that you check it so we can provide as many links to the referenced articles as possible.

17. Please provide issue number for Chandel et al. (2012).

18. Please provide issue number for Ibne Islam et al. (2017).

19. Please provide the publisher or sponsor name and location (not the conference location) for Johnson and Cook (1983).

20. Please provide publisher name for Johnson and Stryk (1987).

21. Please provide the publisher or sponsor name and location (not the conference location) for Lacerda and Lacome (2001).

22. Please provide issue number for Liden et al. (2012).

23. Please provide issue number for Lu and Wen (2018).

24. Please provide issue number for Nechitailo (2015).

25. Please provide the publisher or sponsor name and location (not the conference location) for Plassard et al. (2011).

26. Please provide volume number, issue number and page range for Roy et al. (2016).

27. Please provide the publisher or sponsor name and location (not the conference location) for Schwer (2009).

28. Please provide issue number for Sherburn et al. (2015).

29. Please provide volume number issue number and page range for Wu et al. (2017a).

30. Please provide issue number for Wu and Ren (2015).

31. Please provide issue number for Wu et al. (2017b).

32. A check of online databases year found in this reference. Please Add year '2013'.

33. Please provide issue number for Wu et al. (2014b).

34. Please provide issue number for Wu et al. (2016c).

35. Please provide issue number for Xiao et al. (2017).